České vysoké učení technické v Praze
Fakulta jaderná a fyzikálně inženýrská

Katedra fyziky
Obor: Experimentální jaderná a částicová fyzika

Využití monolitických pixelových detektorů pro kosmickou dozimetrii

An application of monolithic pixel detectors in space dosimetry

BAKALÁŘSKÁ PRÁCE

Vypracoval: Marek Strnad
Vedoucí práce: Ing. Michal Marčišovský, Ph.D.
Rok: 2023

FAKULTA JADERNÁ A FYZIKÁLNĚ INŽENÝRSKÁ
KATEDRA FYZIKY

ZADÁNÍ BAKALÁŘSKÉ PRÁCE

Akademický rok: 2022/2023

Student:	Marek Strnad
Studijní program:	Aplikace přírodních věd
Obor:	Experimentální jaderná a částicová fyzika
Název práce: (česky)	Využití monolitických pixelových detektorů pro kosmickou dozimetrii
Název práce: (anglicky)	An application of monolithic pixel detectors in space dosimetry
Jazyk práce:	Angličtina

Pokyny pro vypracování:

1) Charakterizace kosmického prostředí v cislunárním prostoru
2) Polovodičové detektory záření a principy detekce
3) Vlivy záření na polovodičové struktury
4) Experimentální měření odezvy monolitických křemíkových detektorů

Doporučená literatura:

[1] J.R. Wertz et al., Space Mission Engineering: The New SMAD, Microcosm Press, 2011
[2] G. Lutz: Semiconductor Radiation Detectors, Springer, 1999 3.
[3] G. F. Knoll: Radiation Detection and Measurement, Wiley, 2010 2.
[4] H. Spieler: Semiconductor Detector Systems, Oxford University Press, 2011

Jméno a pracoviště vedoucího bakalářské práce:

Ing. Michal Marčišovský, Ph.D.
Katedra fyziky, Fakulta jaderná a fyzikálně inženýrská ČVUT v Praze

Datum zadání bakalářské práce: 20.10.2022

Termín odevzdání bakalářské práce: 02.08.2023

Doba platnosti zadání je dva roky od data zadání.

....
garant oboru

....
vedoucí katedry

....
děkan

V Praze dne   20.10.2022

ČESKÉ VYSOKÉ UČENÍ TECHNICKÉ V PRAZE
Fakulta jaderná a fyzikálně inženýrská

Břehová 7
115 19 Praha 1

P R O H L Á Š E N Í

Já, níže podepsaný

Jméno a příjmení studenta: Marek Strnad

Osobní číslo: 494719

Název studijního programu (oboru): Experimentální jaderná a částicová fyzika

prohlašuji, že jsem **bakalářskou** práci s názvem:

Využití monolitických pixelových detektorů pro kosmickou dozimetrii

vypracoval samostatně a uvedl veškeré použité informační zdroje v souladu s Metodickým pokynem o dodržování etických principů při přípravě vysokoškolských závěrečných prací.

V Praze dne 2. 8. 2023

....

podpis

Acknowledgement

Název práce:

Využití monolitických pixelových detektorů pro kosmickou dozimetrii

Autor:	Marek Strnad
Studijní program:	Aplikace přírodních věd
Obor:	Experimentální jaderná a částicová fyzika
Druh práce:	Bakalářská práce
Vedoucí práce:	Ing. Michal Marčišovský, Ph.D.
	Katedra fyziky, Fakulta jaderná a fyzikálně inženýrská ČVUT v Praze
Konzultant:	–

Abstrakt: Tato práce se zaměřuje na analýzu nejnovějších experimentů, provedených na testování využitelnosti detektoru SpacePix-3 pro budoucí vesmírné mise, jako například mise LVICE^2. První experiment se zabýval měřením odezvy detektoru SpacePix-3 vůči iontovému svazku o energii 290 MeV/u na urychlovači HIMAC pod třemi různými úhly svazků k povrchu detektoru (0°, 80°, a 90°). Druhý experiment mapoval radiační prostředí Země využitím SpacepiX Radiation Monitoru (SXRM) na palubě nanodružice VZLUSAT-2, orbitující na heliosynchronní orbitě.

Klíčová slova: vesmírné prostředí, křemíkové detektory, SpacePix, HIMAC, VZLUSAT-2

Title:

An application of monolithic pixel detectors in space dosimetry

Author:	Marek Strnad

Abstract: This work focuses on the analysis of the latest experiments, conducted to test the applicability of the SpacePix-3 detector for future space missions, such as the LVICE^2 mission. The first experiment was to measure the SpacePix-3 response to the HIMAC 290 MeV/u Si beam under three different beam angles in regards to the detector plane (0°, 80°, and 90°). The second experiment was mapping out the Earth's radiation environment using the SpacepiX Radiation Monitor (SXRM) onboard the VZLUSAT-2 nanosatellite orbiting in sun-synchronous orbit.

Key words: space environment, silicon detectors, SpacePix, HIMAC, VZLUSAT-2

Contents

Introduction

Space exploration has been humanity's desire since the dawn of time, but only in the last few hundred years has it become a reality. The Moon, in particular, has piqued the most interest, for it is the closest cosmic body in our vicinity. Many great advancements in reaching the Moon have been made since the creation of the first telescopes, such as the first outer space flight, the first object in orbit, and finally, the first human to walk on the Moon. In recent years, however, the focus shifted from crewed landing missions to the research of the cis-lunar space environment, using satellites, probes, and other uncrewed spacecraft, with hopes of developing and testing the technology needed for the Artemis[1] and Lunar Gateway[2] missions.

One of these is the LVICE[2] probe. It is the first purely Czech mission to reach the Moon and explore the cis-lunar space environment, where it will study dust concentration, radiation, and the plasma environment. LVICE[2] will carry multiple scientific instruments to fulfill its mission goals. These instruments need to be small, accurate, reliable, and durable. One of these instruments, the SpacepiX Radiation Monitor, SXRM, contains SpacePix-3 chips, monolithic active pixel detectors. These chips have been developed at the FNSPE CTU[3] and are being tested with the mission requirements in mind.

The main goals of this thesis are segmented into four chapters. The first two chapters are about the physics background for understanding the problematics of space dosimetry. In Chapter 1, the space environment is introduced, and different environments, such as radiation or plasma and other spacecraft-affecting effects, are characterized.

Semiconductor detectors are the topic of Chapter 2. Together with describing semiconductors themselves, basic semiconductor structures, and pixel detectors, namely SpacePix-2 and 3, the electron-hole pair production in semiconductors necessary for signal generation, and radiation effects on semiconductor detectors are also discussed.

---

[1] https://www.nasa.gov/specials/artemis

[2] https://www.nasa.gov/gateway

[3] Faculty of Nuclear Sciences and Physical Engineering of the Czech Technical University in Prague

The two remaining chapters are regarding the analysis of two recent SpacePix experiments. The first experiment, which is presented in Chapter 3, was irradiation of the SpacePix-3 detector by the HIMAC 290 MeV/u Si beam, using 0°, 80°, and 90° angles of inclination to test the detector's response to the particle beams, entering at different angles with respect to the detecting chip.

The last chapter, Chapter 4, is about analyzing the results of a 24 hour measurement of the Earth's radiation environment, utilizing the SpacepiX Radiation Monitor, SXRM, on board the VZLUSAT-2 nanosatellite orbiting in low Earth orbit. This chapter is closed out by introducing the upcoming LVICE² mission and the part SpacePix detectors play in it.

Chapter 1

Space environment

Based on our perspective from Earth, the space environment is defined as a region beyond Earth's atmosphere, where a non-terrestrial space environment can affect spacecraft functionality. This area consists of the near-Earth space environment, which is made of upper levels of Earth's atmosphere, a lower boundary proposedly defined by the Kármán line[1], and the deep space environment, extending beyond the heliosphere.

When considering orbitally bound spacecraft, the Earth's space can be divided into several orbits. The low Earth orbit, LEO, spans from 160 km to 2000 km above sea level, and it is where most of the satellites are [1]. The ISS and the Hubble telescope also orbit there. The medium Earth orbit, MEO, and the high Earth orbit, HEO, are separated by a border of geosynchronous orbit, GSO, which is 35786 km above sea level [1], where satellites orbit Earth at the same rate that the Earth rotates. Orbiting in GSO above the equator results in a fixed location of satellites in the sky as observed from Earth. This type of GSO is called the geostationary orbit, GEO. The MEO is home to semi-synchronous satellite navigation systems, such as GPS, Galileo, and GLONASS, and the GEO is to communications, weather, and other navigational satellites.

In near-Earth space, there are several components of space environment with detrimental effects to spacecraft, ranging from the effects of Earth's captured radiation environment field through spacecraft interactions with reactive atmospheric atoms and man-made space debris. The altitude dependence of these effects can be seen in Fig. 1.1, and they will be described in this chapter.

---

[1]Kármán line is a proposed boundary separating Earth's atmosphere and outer space. It has no physical meaning and is set to 100 km above sea level.
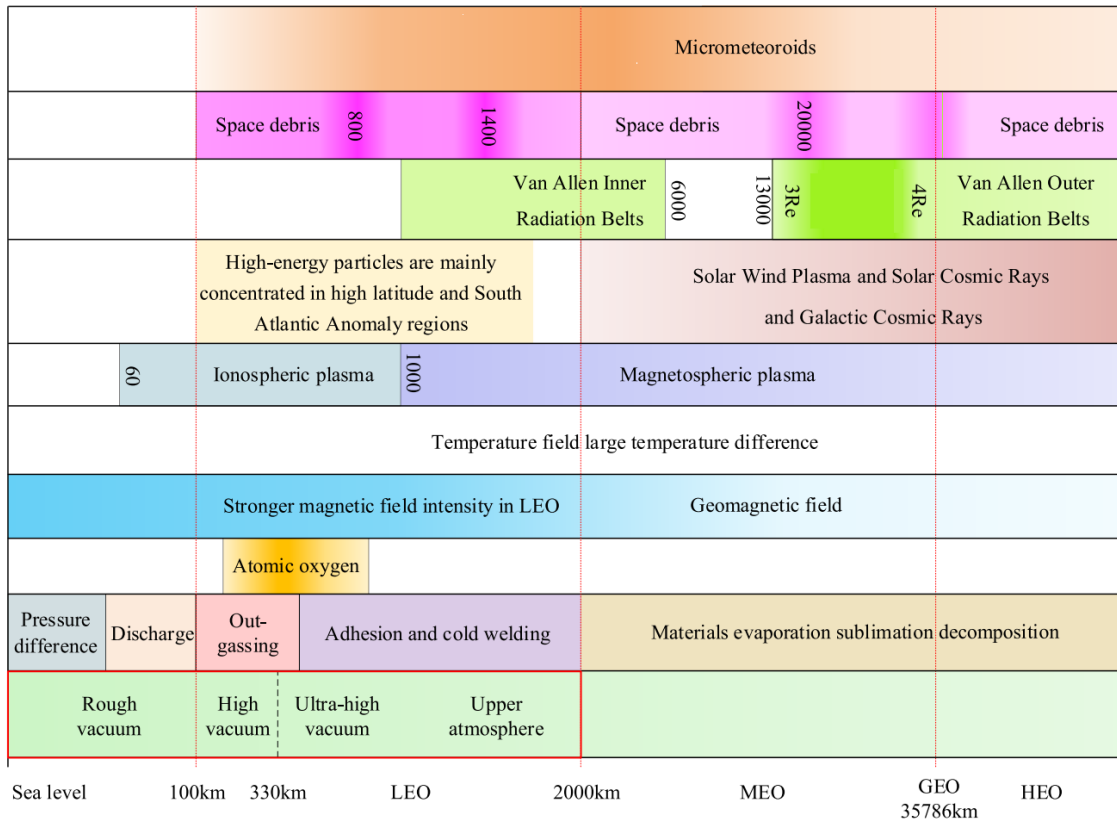
Micrometeoroids

Space debris | 800 | 1400 | Space debris | 20000 | Space debris

Van Allen Inner Radiation Belts | 6000 | 13000 | 3Re | 4Re | Van Allen Outer Radiation Belts

High-energy particles are mainly concentrated in high latitude and South Atlantic Anomaly regions

Solar Wind Plasma and Solar Cosmic Rays and Galactic Cosmic Rays

60 | Ionospheric plasma | 1000 | Magnetospheric plasma

Temperature field large temperature difference

Stronger magnetic field intensity in LEO | Geomagnetic field

Atomic oxygen

Pressure difference | Discharge | Out-gassing | Adhesion and cold welding | Materials evaporation sublimation decomposition

Rough vacuum | High vacuum | Ultra-high vacuum | Upper atmosphere

Sea level | 100km | 330km | LEO | 2000km | MEO | GEO 35786km | HEO

Figure 1.1: Components of the space environment, discussed in Chapter 1, in their respective altitudes. Re $\approx$ 6378 km is the Earth's radius. Color gradient in certain components represents the increasing or decreasing severity of their effects. Darker color means higher severity. Taken and edited from [1].

1.1 Plasma environment

Spacecraft can come in contact with charged particles in the form of a plasma environment. In Earth's space, this consists of ionospheric plasma, magnetospheric plasma, and solar wind plasma. These types of plasmas are created by interactions of solar radiation, geomagnetic field, and upper atmospheric particles. The solar wind beyond Earth magnetosphere can be also described as plasma and it will be shortly discussed in a separate section.

Solar photons of UV and X-ray energies can to strip electrons from gas atoms in the upper atmosphere. This creates an abundance of electrons and ions on the dayside of Earth, which dissipates during the night when electrons and ions recombine into their original neutral molecules. During the day, however, this is how the sunlight-conditioned ionosphere is created. These charged particles are then affected by the geomagnetic field, which causes them to create the equatorial anomaly, which is a region of peak plasma density located between $\pm$ 10° and 20° latitudes, as shown in Fig. 1.2.
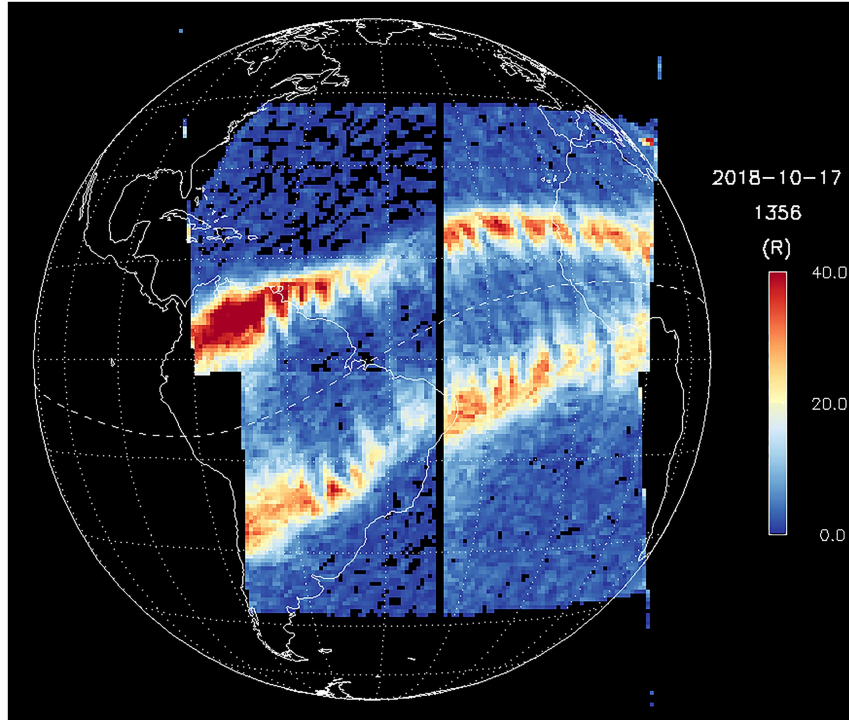
Figure 1.2: Visualisation of the equatorial ionization anomaly measured by the Global-scale Observations of the Limb and Disk mission from 17. October 2018. R is a unit of photon flux, the Rayleigh, defined as 10^6 photons cm^{-2}s^{-1} emitted in all directions. Taken from [2].

Upon interaction with satellites, these charged particles can cause surface charging, resulting in electrostatic discharges, electronic pulse jamming, short circuits, and material performance degradation. Even the smallest discharges can degrade and permanently damage the electromagnetic components of satellites. As a defense against this, grounding and electromagnetic shielding are used, along with materials with lower resistivity that help with continuous electric charge movement in the spacecraft surface materials.

1.2 Radiation environment

Of all the space environments, the radiation environment has the most significant influence on spacecraft, causing around 40% of anomalies [3]. This is one of the reasons for measuring the radiation environment. Others can be human health protection, protecting future cosmonauts leaving the Earth from radiation damage, and better understanding the incoming space radiation itself. The radiation environment is primarily composed of protons, electrons, heavy nuclei, and neutrons. The primary sources are both solar and galactic cosmic rays, the particle cascades they induce by interacting with the Earth's atmosphere, and Van Allen radiation belts, as can be seen in Fig. 1.3. Along with surface charging similar to the plasma environment,

these particles can cause many problems, such as sputtering, single-event phenomena, and spurious event creation.
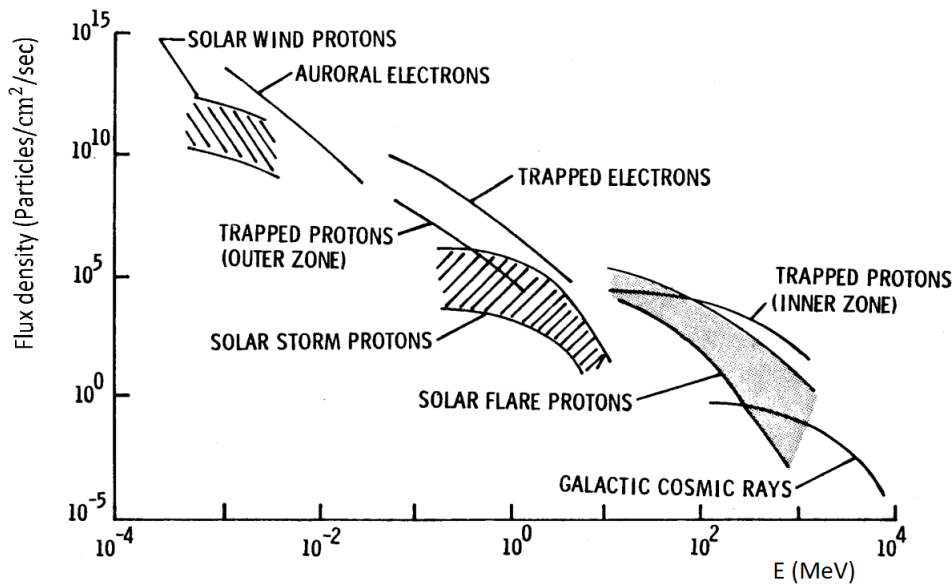

Figure 1.3: Sources of radiation and plasma based on its flux density and energy. Taken from [4].

Solar cosmic rays, SCR, are a flux of charged particles that come to us from the Sun and are created in Solar particle events, which occur in association with solar flares. Most of these particles are protons [5] with energies ranging from 1 MeV to 1 GeV [6], but electrons and helium nuclei are also present. Galactic cosmic rays, GCR, are similar to SCR, except they originate outside our solar system and consist of heavier nuclei and protons. They have multiple possible sources, with supernova explosions being the most probable. Despite having higher energies than SCR, their flux is much lower, resulting in a satellite interaction being a much rarer occurrence. The flux of galactic cosmic rays drops with increasing particle energy, as is shown in Fig. 1.4. As the solar activity[2] fluctuates, so does the flux of GCR. Higher solar activity results in a lower GCR flux. It is caused by the change of the interplanetary magnetic field [7]. This effect is called the GCR modulation. Similarly, the GCR flux also decreases after a coronal mass ejection erupts. This effect is called the Forbush decrease.

Not all secondary charged particles created by cosmic ray showers in the upper atmosphere reach ground, some will get deflected and even captured by Earth's geomagnetic field, especially those primary GCR particles which are only grazing the planetary atmosphere. A high concentration of these captured high-energy particles forms the Van Allen radiation belts in which they are non-uniformly distributed. There are typically two Van Allen radiation belts around Earth, the inner radiation

---

[2]Solar cycle is a periodic change of the Sun's activity, regarding emitted radiation and the number and size of solar events
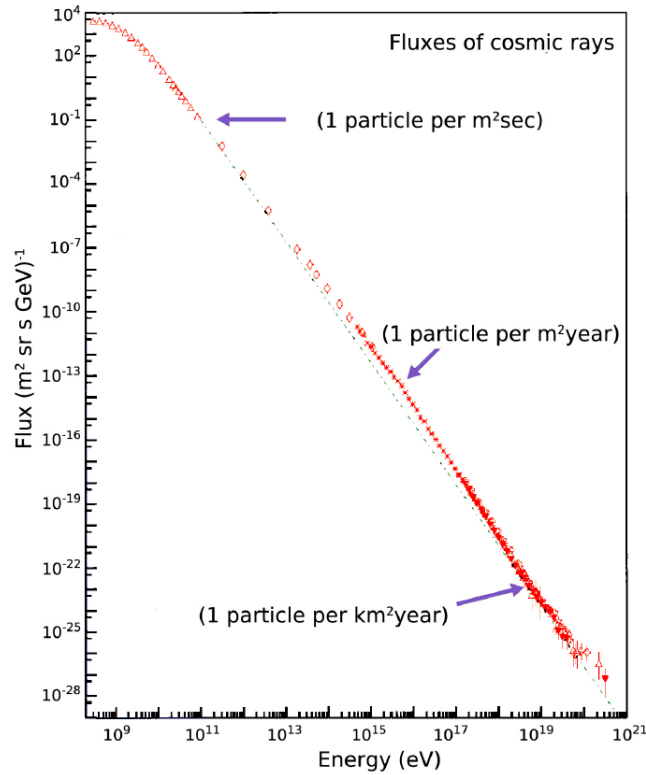
Figure 1.4: The spectrum of cosmic ray flux. It quickly decreases with increasing energy. Particles with the highest flux in this figure are mostly of solar origin, the medium flux is mainly galactic cosmic rays, and the lowest flux is of extragalactic cosmic rays. Taken from [8].

belt, and the outer radiation belt. Both can be seen in Fig. 1.5. Other Van Allen radiation belts, temporary belts, can also exist and form after certain solar particle events or even nuclear explosions when detonated in space. The inner radiation belt ranges from 600 km to 10000 km, and it is stable because of its shielding by Earth's magnetic field against solar events. High-energy protons are the main components. These protons are a product of neutron beta decay, where the neutrons are created by high-energy cosmic ray collisions in the atmosphere. The outer radiation belt spans from 13000 km to 45000 km, is much less stable, and is mainly comprised of high-energy electrons. Being less stable means that the absolute intensity of electrons fluctuates at short intervals [9]. Because of the Earth's magnetic axis deviation from the rotational axis, the Van Allen radiation belts are also deviated, resulting in the emergence of the South Atlantic Anomaly. It is an area where the inner radiation belt is closest to Earth's surface, caused by a decrease in Earth's magnetic field (seen in Fig. 1.6), which increases the flux of energetic particles in LEO. The anomaly is located above the southern part of the Atlantic Ocean and South America and poses a significant threat to all spacecraft passing through because of its ability to damage electronics, and it is also a hazard for any astronauts there [10].
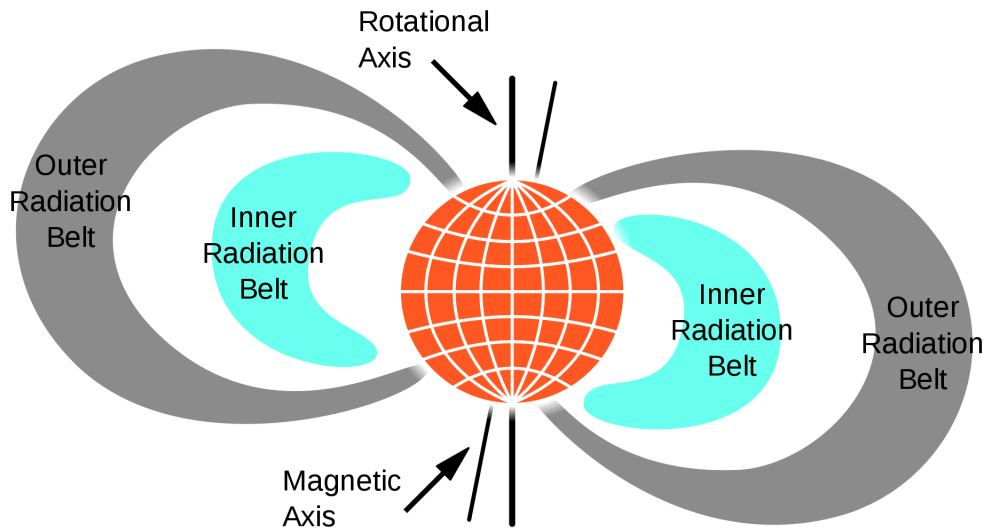
7

Figure 1.5: Visualisation of inner and outer Van Allen radiation belts. Taken and edited from [11].

Particles from the space radiation environment are usually more damaging than the ones in the plasma environment, mainly because they are more energetic, meaning they can penetrate the spacecraft's surface and cause displacement charges, internal charging, and even radiation damage. The single-event effects, SEEs, are electronic disruption effects resulting from a single particle interaction. More on SEEs in the Section 2.4. Even without penetrating the spacecraft surface, these energetic particles can bombard and do physical damage to spacecraft construction components. This effect is called sputtering.

1.3   Macroscopic particles

The space around Earth is filled with various macroscopic particles that can be divided into two categories based on their origin. Space debris is made by human space activities, and micrometeoroids come from asteroids and comets. These particles can pose a danger to all spacecraft because collisions with even the small-size debris can have detrimental repercussions due to its orbital velocity. Even a millimeter-sized meteoroid at 20 km/s has equivalent energy to a baseball bat swing [13]. A result of a laboratory experiment with micrometeorite analogs can be seen in Fig. 1.7.
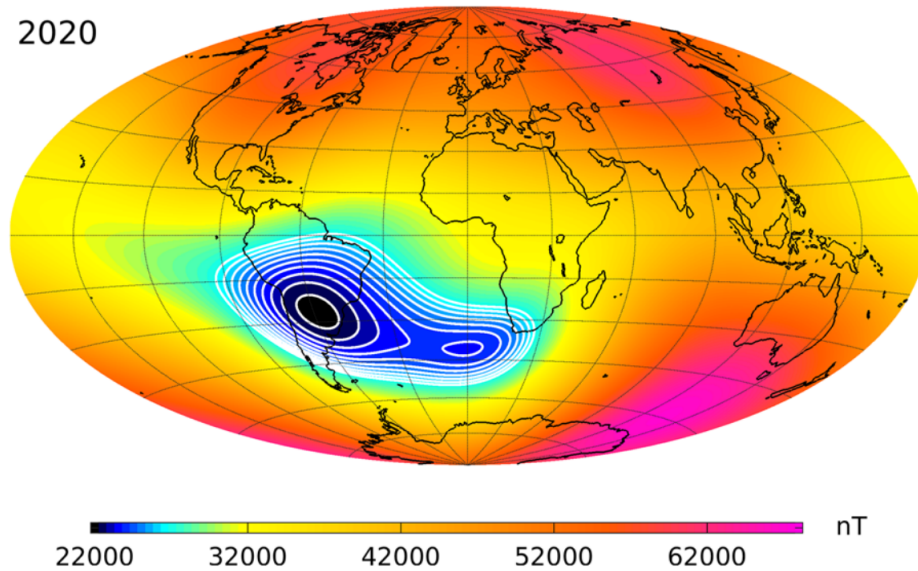
Figure 1.6: The strength of Earth's magnetic field with the location of the South Atlantic Anomaly visible. Taken from [12].
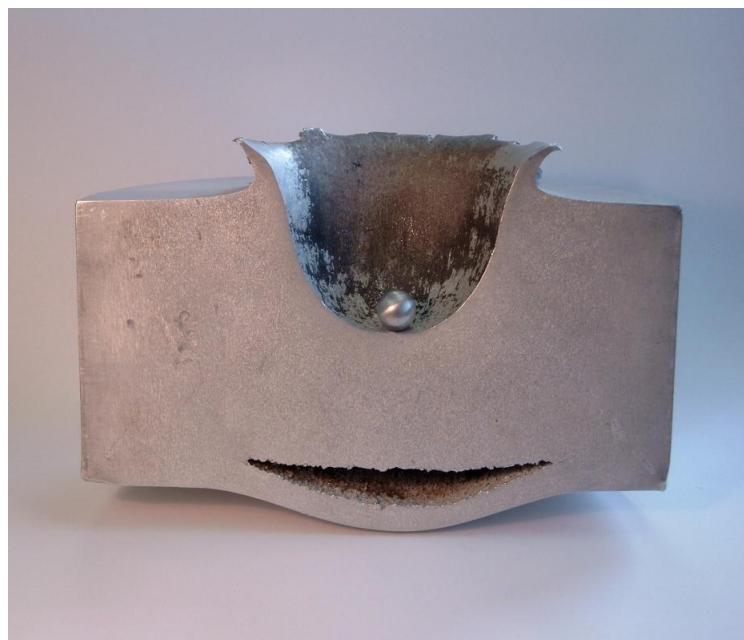

Figure 1.7: A lab test collision result of an aluminum sphere with a diameter of 1.2 cm traveling at approximately 6.8 km/s striking an aluminum block. A crater with a depth of 5.3 cm was created, and a spall formed at the opposite end. Taken from [18].

Space debris is categorized by its size into three groups. The large-sized debris, having more than 10 cm in diameter, is the most damaging of all three but has the smallest flux [14]. The small-sized debris has less than 1 cm in diameter. This type of debris has the highest flux of these three and can still cause physical damage,

similar to sputtering in the previous section. It can also degrade surface electronics, such as solar panels [14], and because of its size is difficult to be tracked or observed. The third type is debris with a diameter between 1 cm and 10 cm. The amount of space debris depends on altitude and has been increasing rapidly in recent years. This increase can be seen in Fig. 1.8. This number can reach critical values when cascade space object collisions would make the orbit inoperable. This theoretical scenario is called the Kessler syndrome [15]. The spatial distribution of space debris orbiting in different orbits can be seen in Fig. 1.9.
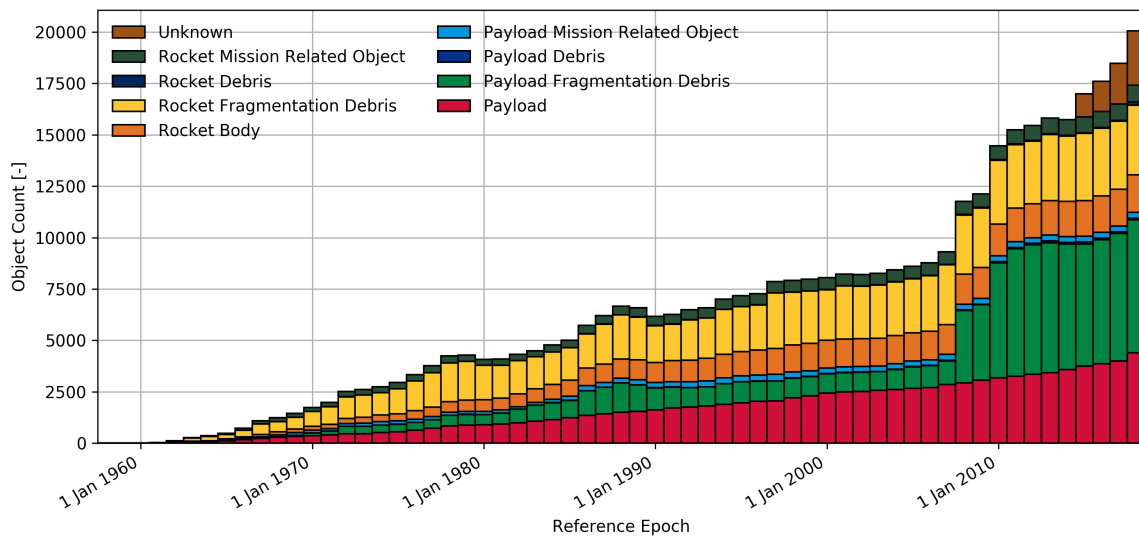
Figure 1.8: Time evolution of the amount of different types of space debris. An increase in unknown types of debris in recent years can be seen. Taken from [16].

In comparison to space debris, micrometeoroids are not gravitationally bound to Earth, and they might strike spacecraft from any direction. They have lower altitude-dependant average flux than space debris but can reach higher velocities, 20 km/s on average and even 70 km/s in special cases [13].

Macroscopic particles can cause three main types of damage with hypervelocity impacts, which are defined as impacts with relative velocity in excess of 3 km/s. The first one is erosion. It is the most frequent out of all three. It causes surface craters with the size in the order of μm and can also degrade the performance of hit electronic devices, such as solar panels. The second one is penetration, which can range from small, when it damages non-crucial components, to catastrophic, when it punctures essential parts, such as a fuel tank. The last type is destruction, which, as the name suggests, leads to catastrophic mission failure but is the rarest of all three.

10

Figure 1.9: Visualisation of different types of space debris orbiting Earth with data about objects larger than 10 cm comes from the US Space Surveillance Catalogue, and for smaller objects from a statistical model made by ESA. Red dots represent satellites, yellow dots rocket bodies, green dots mission-related objects, and blue dots fragments. Different orbits, such as LEO and GEO, are visible, with LEO closely surrounding the Earth, while GEO spans furthest away. Taken from [17].

1.4 Other effects

Outside of these three major space environment contributors, there are still multiple other sources of space hazards. They can be divided into multiple categories, atmospheric effects such as drag and atomic oxygen, vacuum, solar activity, and geomagnetic field.

Atmospheric drag
Even at high altitudes, there are still enough atmospheric particles to produce a drag on passing spacecraft. This can affect the slope and altitude of orbits and lower the lifetime of orbit. The drag highly varies with solar activity and atmospheric changes and decreases rapidly in altitudes above 400 km [19].

Atomic oxygen
Earth's atmosphere consists of 20.95% oxygen, normally in the form of O_2 molecules [20]. These molecules can, however, be split by electromagnetic radiation or by ionization, creating atomic oxygen O. At surface altitudes, individual atoms quickly reform a molecule, but at higher altitudes, they do not because of the small spatial density of particles. This atomic oxygen causes oxidation weakening materials and degrading electronics' performance [21].

Vacuum

Even in the uppermost parts of Earth's atmosphere, there is still no complete vacuum. Despite being just ultra high-vacuum, it can still have several effects on spacecraft. Firstly, out-gassing is a release of gaseous chemical compounds from solid materials, which were used during spacecraft component manufacturing. It can have detrimental effects, especially on optical components. Secondly, cold welding is an effect, where the ultra-high vacuum sucks out even the tiny spaces of air between mechanical parts, causing them almost to weld together. This makes them almost immovable in regard to each other. Thirdly, in a vacuum, the only type of heat transfer of an object with its surrounding is by radiation. This causes satellites to undergo fast temperature gradients because of the Sun heating and space cooling contrast. This also removes the possibility of cooling electronics using convection which is one of the main problems for electronics in space. All of these effects can cause multiple types of spacecraft material degradation [22].

Solar events

A solar storm is a release of energy in the form of electromagnetic radiation, high-energy particles, and plasma clouds. There are several types of solar events. A solar flare is an eruption in Sun's atmosphere above sunspots, releasing electromagnetic waves into surrounding space. A solar flare can release such a powerful X-ray burst, blinding electronic sensors and exciting the ionosphere, making low-frequency communication impossible [23]. Solar flares are sometimes accompanied by coronal mass ejections, CMEs, which can release large clouds of magnetised plasma into interplanetary space. Some of the charged particles can be accelerated in the shockwave and reach relativistic velocities. The pressure from these particles can have similar effects on spacecraft as atmospheric drag, except smaller [24]. A disturbance in Earth's magnetic field caused by the more prominent solar events is called a geomagnetic storm. These storms can disturb the upper levels of Earth's atmosphere and can lead to irreparable damage to spacecraft [24].

Chapter 2

Semiconductor detectors

Semiconductor detectors are ionizing radiation detection devices made from solid semiconductors. They have several significant advantages over gaseous phase and scintillation detectors. They can be much thinner than gas-based ionization chambers due to solid matter having a larger density than gas, and they also directly produce charge carriers in comparison to scintillation detectors, which need additional methods to detect scintillation photons. Other benefits of semiconductor detectors are their relatively fast timing characteristic and the possibility of using already existing processes in microelectronic silicon foundries for detector manufacturing. The disadvantages of silicon detectors are that they are expensive and that they can be sensitive to radiation damage. In the case of semiconductor detectors, signal is formed from electrons and holes produced by ionizing radiation in the material, which is different from ions and free electrons, that carry electric current in gas-phase detectors. The most commonly used materials are silicon and germanium, where germanium is used mainly for gamma ray spectroscopy and silicon is used for the detection of charged particles and soft X-rays. Among the new perspective materials are CdTe, with applications in x-ray and gamma ray detectors, and 4H-SiC and GaN for charged particle detectors because of their radiation tolerance.

2.1   Semiconductors

The periodic crystal lattice of atoms inside materials allows for electron energy bands to exist. There is a valence band, where electrons are bound to the lattice, and a conduction band, where electrons are free to move through the crystal. The electron energy must fall within these bands, resulting in a band gap, the forbidden band. The size of this gap determines the type of material. Metals have valence and conduction bands that overlap, meaning that there is a zero gap between them, resulting in an electron being able to move between bands to conduct electric current. Insulators and semiconductors both have a band gap, but insulators have it much wider. Silicon, for example, has a band gap of 1.14 eV [25], while silicon dioxide

has a band gap of 9.3 eV [26]. This implies that at low temperatures, both have all electrons situated in the valence band, but with temperature increasing, electrons in semiconductors can get thermally excited into the conduction band more easily than in insulators. Once the electron is excited into the conductive band, it leaves a hole in the valence band, resulting in the creation of an electron-hole pair. This pair migrates in an electric field the same way an ion pair would, meaning it can conduct an electric current. The difference in band gaps between different classes of materials can be seen in Fig. 2.1.
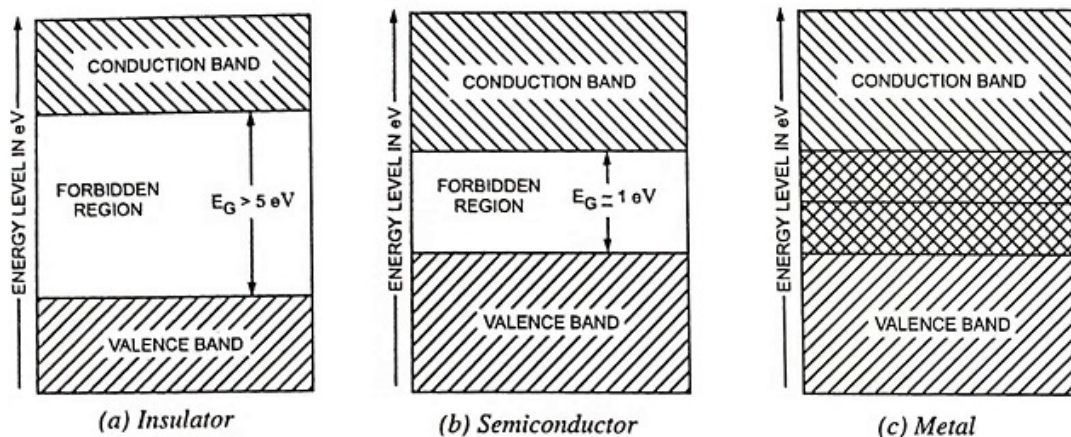
Figure 2.1: Energy band diagrams of insulators (a), semiconductors (b), and metals (c). Figure from [27].

Intrinsic semiconductors are completely pure semiconductors in which all electron-hole pairs are created only by thermal excitation. They are rare, however, because even the smallest impurity or defect can affect desired properties. Manually adding impurities into semiconductors, also called doping, is used to create n-type and p-type semiconductors. For example, if a small impurity of phosphorus, with phosphorus atoms having five valence electrons, was added into silicon with four valence electrons per atom, an n-type semiconductor with a free valence electron would be created. Because this electron is not from the crystal lattice, its energy resides in the forbidden band, just below the conduction band. This proximity causes the electron to be easily thermally excited into the conduction band and be able to move in the lattice. This does not change the overall charge neutrality, as it also creates a positively charged donor. A similar effect would happen if boron with three valence electrons per atom was added, except this would create a p-type semiconductor. In this case, there would be an absence of an electron in the valence band, called a hole. Potential electrons in this position would also have an energy level in between the allowed bands, except just slightly above the silicon electron valence band. This results in the electron being able to move to the acceptor level after thermal excitation, creating a hole in the valence band. If we were to add higher than usual concentrations of impurities, we would create heavily doped materials, n^+-type and p^+-type, which would be more conductive than the ordinary doped materials. These heavily doped

14

regions are useful for the creation of electric contacts in semiconductors because the emergence of Schottky junctions between metals and semiconductors is suppressed.

2.2   Basic semiconductor structures

By combining the p-type and n-type semiconductors, we create a p-n junction. While both types are without an electric charge, the p-type has a lot higher hole density and the n-type has a lot higher electron density than their counterparts. Adding them together results in electron and hole diffusion into each other to equalize the concentrations. Holes start moving into the n-type, electrons into the p-type, and they start to recombine around the junction, creating a depleted region. This, however, disrupts the charge neutrality and causes the depleted region in n-type to gain a net positive charge and the depleted region in p-type to gain a net negative charge, resulting in an electric field in the opposite direction of the diffusion, thus impeding it. The diffusive force and the electric force create equilibrium after a while. This principle can also be seen in Fig. 2.2. The depleted region can then be used as a detector, in which an ionization particle creates electron-hole pairs in the depleted region, with electrons and holes both drifting in opposite directions in the electric field, creating a measurable current. This method is, however, not very effective, mainly because the electric field is too small to move charge carriers quickly and also because the depleted region is too small in comparison to the rest of the crystal.
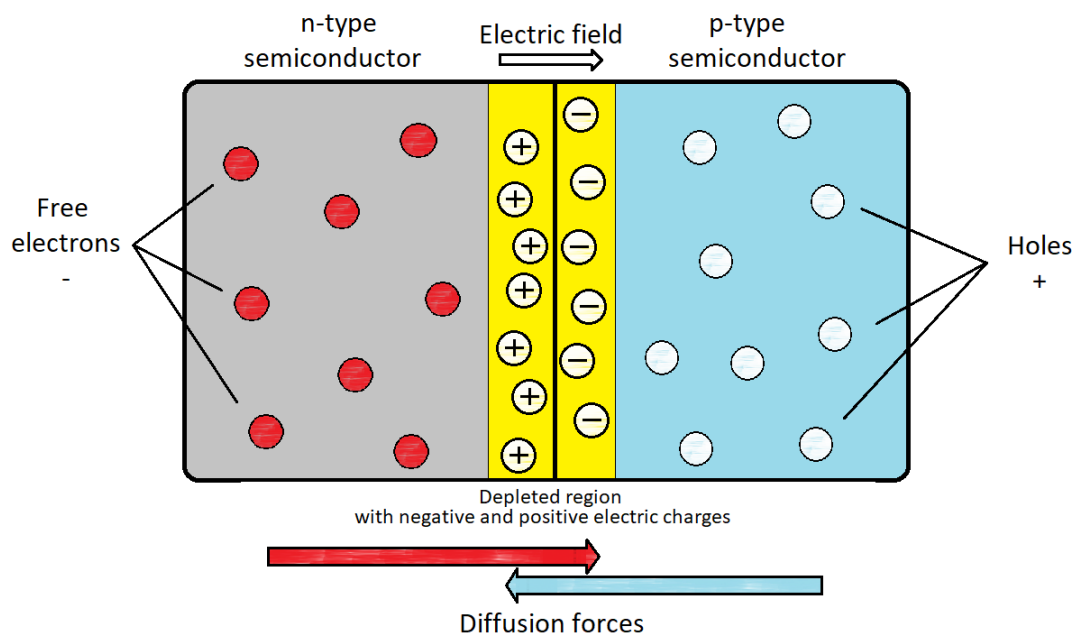

Figure 2.2: Schematic view of an unbiased p-n junction, where both n-type and p-type semiconductors have a neutral net charge, but the depleted region gains both charges, resulting in an electric field.

Because of this, we use reverse bias, which means connecting an external voltage source to the p-n junction, negative to the p-type and positive to the n-type, so that it has the same direction as the electric field inside. This has mainly two effects: it widens the depleted region and amplifies the diffusion-stopping voltage, eliminating both of the aforementioned problems of particle detection using the p-n junction.

The same diffusion mechanism can also happen in n^+-n or p^+-p junctions, except only electrons or holes move from heavily doped materials, still resulting in an electric field counteracting the diffusion. n^+-n or p^+-p are called homojunctions. These junctions are often ignored in the analysis of devices.

2.3 Pair generation in semiconductor detectors

In order to measure an ionization signal using semiconductor detectors, we need the incoming particles to create electron-hole pairs. This can be done by exciting electrons from the valence band to the conductive band. There are three main ways of pair creation: thermal agitation, optical excitation, and ionization. Electrons and holes are always created in pairs, independently of the energy or type of incident particle or the structure and composition of the semiconductor. Every excited electron must leave a hole in the valence band in its place.

2.3.1 Thermal agitation

Certain semiconductors, such as Ge (band gap of 0.66 eV [25]), can have such a small band gap that them being at room temperature can be enough to excite electrons to the conduction band. This thermal agitation creates background noise but can be removed by lowering the temperature to cryogenic levels, most commonly to the temperature of evaporating liquid nitrogen. Other semiconductors, such as Si and GaAs, with larger band gaps, can still suffer from thermal agitation because of impurities and their intermediate local states in the band gap.

2.3.2 Optical excitation

When an optical photon is absorbed by the semiconductor, the surplus energy can be enough to excite an electron. If it has more than enough energy, the excited electron first has to transfer it to the lattice via mechanical vibrations, or phonons. This optical excitation is used in photodiodes and solar cells.

2.3.3 Ionisation

Typically, the ionizing radiation particles are grouped into four groups: heavy charged particles, electrons, high-energy photons, and neutrons. The first two carry an electric charge, meaning they interact with electrons in a semiconductor through elastic collisions, in which they transfer a portion of their energy to the electron, exciting it to the conduction band with the electron leaving a hole behind. With external voltage applied, both electrons and holes drift to their respective electrodes, creating a measurable electrical signal. The last two, on the other hand, carry no electric charge, so additional processes need to happen for them to be detectable. The benefit of semiconductor detectors is the small amount of ionization energy that needs to be deposited. For silicon, it is 3.6 eV, and for germanium, it is 2.9 eV, approximately ten times less than in gas-filled detectors [28].

Heavy charged particles
The energy transfer from a heavy charged particle, such as protons and heavier nuclei, to electrons in a semiconductor is best described by the Bethe-Bloch formula:

$$\left\langle -\frac{\mathrm{d}E}{\mathrm{d}x} \right\rangle = 4\pi N_A r_e^2 m_e c^2 \frac{Z}{A} \frac{z^2}{\beta^2} \left[\frac{1}{2} \ln \left(\frac{2m_e c^2 \beta^2 \gamma^2 W_{max}}{I^2} \right) - \beta^2 - \frac{\delta(\beta\gamma)}{2} \right], \quad (2.1)$$

where N_A is Avogadro's constant, r_e classical electron radius, m_e electron mass, c speed of light, Z atomic number of absorber, A atomic weight of absorber, z charge of incident particle, W_{max} maximum energy transfer in a single collision, δ density-effect correction, and $\gamma = \frac{1}{\sqrt{1-\beta^2}}$ with $\beta = \frac{v}{c}$, taken from [29]. The function is also visible in Fig. 2.3.

Electrons
Electrons are excluded from heavy charged particles due to their mass being ≈ 2000 times lower than that of protons. This causes them to emit photons of X-ray energies via bremsstrahlung upon decelerating due to their deflection on other charged particles, such as nuclei. Electrons can again create electron-hole pairs through elastic scatterings with electrons in the semiconductor, the same way as heavy charged particles, but the Bethe-Bloch formula describing the energy loss needs to be modified to account for the bremsstrahlung.

X-rays and gamma rays
Photons mainly interact with matter in three ways: the photoelectric effect, Compton scattering, and electron-positron pair creation. Cross section of these effects is shown in Fig. 2.4. The photoelectric effect occurs when a photon interacts with an atom and gets absorbed by the atom, which then ejects an electron. Compton scattering is the scattering of an incoming photon with an electron, to which it transfers a part of its original energy. Electron-positron pair production is an effect in which, as the name suggests, a photon vanishes and creates an electron-positron pair. This effect can only take place in the vicinity of a third body, such as a nucleus. Electrons
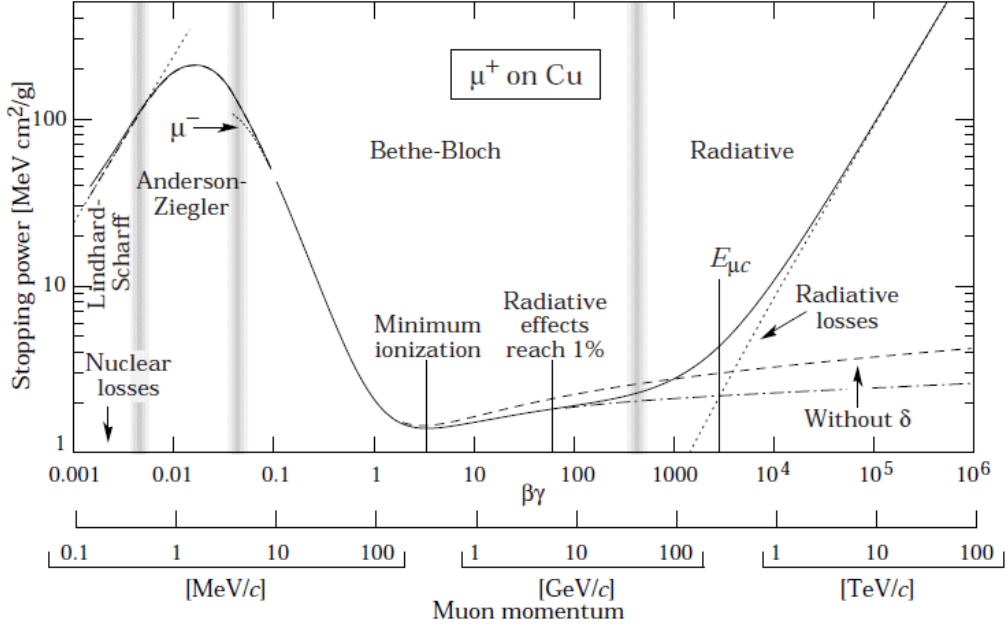
Figure 2.3: Energy transfer for positive muons in copper as a function of the muon momentum. The Bethe-Bloch formula Eg. 2.1 describes the energy loss for the momenta of few MeV/c to tens of GeV/c until the radiative energy losses become more prominent than the ionization losses. The version of the function without the density-effect correction is also visible. Taken from [29].

and positrons created by photon interactions with matter can later create electron-hole pairs, as mentioned above. In semiconductor detectors, Compton scattering is suppressed due to the lack of free electrons in the depleted region. High energy gamma ray can also be absorbed by a nucleus, which then enters an excited state, resulting in the emission of possibly multiple protons and neutrons.

Neutrons

As neutrons cannot interact by Coulomb force, they can be detected only by elastic or inelastic scattering or by nuclear reaction. Elastic scattering of a neutron on a nucleus causes the neutron to transfer a portion of its energy to the nucleus. When a neutron interacts with a nucleus via inelastic scattering, the neutron gets absorbed, putting the nucleus in an excited state, resulting in the nucleus emitting either an electron or a photon. The nuclear reaction causes the nucleus interacting with the neutron to undergo transmutation into a different element. To detect neutrons with silicon detectors, a conversion layer needs to be added to the detector. Conversion layers can be made from ^{6}LiF and ^{10}B for thermal neutron (0.025 eV) capture or polyethylene for fast neutron (> 1 MeV) detection.
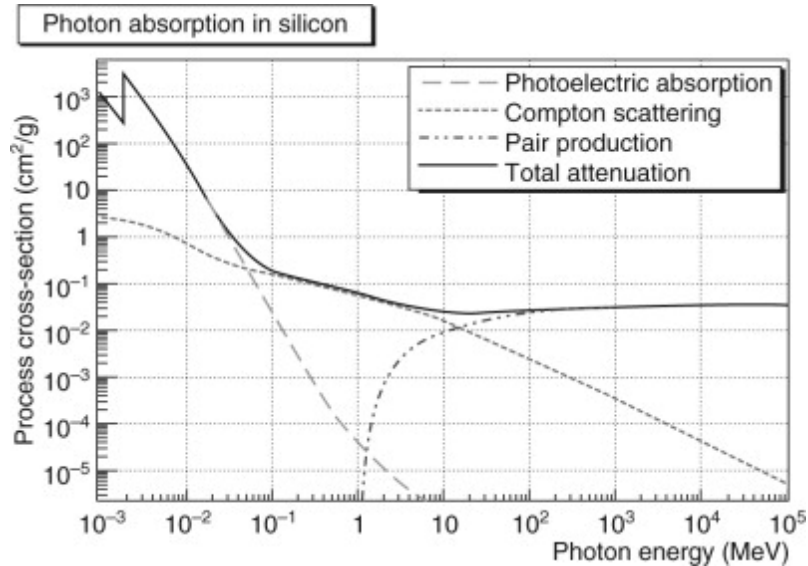
Figure 2.4: Cross section of photon absorption in silicon as a function of the photon energy. The photoelectric effect dominates at the lowest energies. Compton scattering then starts being the main type of photon interactions with matter until the photon energy gets higher than the mass of two electrons, enabling electron-positron pair production to happen and to be the most prominent afterward. Taken from [30].

2.4   Radiation effects on semiconductor detectors

As mentioned in Section 1.2, radiation has the ability to damage and even destroy electronics. This is also the case for semiconductor detectors, thus creating the most radiation-resistant detectors is crucial, especially in space dosimetry. Radiation can have both cumulative effects and single-event effects, SEEs.

Cumulative effects
There are two main types of cumulative effects, depending on the type of interaction. Total Ionizing Dose, TID, and displacement damage, or Non-Ionizing Energy Loss, NIEL. The overall effect is, however, usually a combination of both [28]. Ionization damage happens when an incoming ionizing particle creates free charge carriers. While electrons quickly move to the positive electrode, holes move slowly and pile up on the read-out oxide silicon interface of the MOS structure, shown in Fig. 2.5. This charge accumulation then causes a voltage shift, which then has to be accounted for, increasing the needed input power. It can also create a leakage current, reduce signal gain, and increase background noise and dark current, depending on the type of detector technology [31].

Displacement damage is caused when an incoming particle mechanically dislodges a silicon atom from its lattice site. The dislodged atom then displaces others in its vicinity, creating defect clusters. The displacement damage is not proportional to the deposited energy but mainly depends on the incoming particle type. The defect clusters then cause the formation of mid-gap energy states in surrounding atoms,
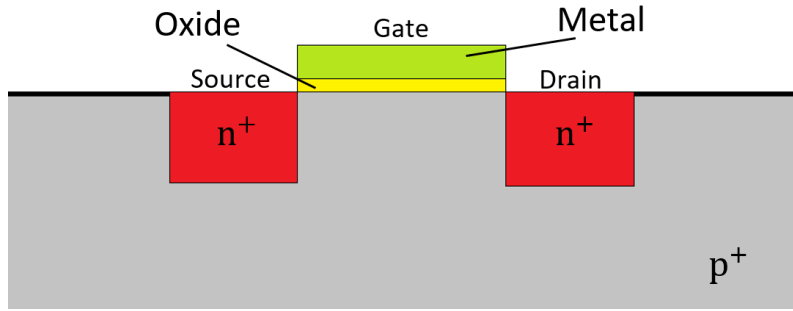
19

Figure 2.5: Cross section of a metal-oxide-semiconductor, MOS, structure, is created by adding a non-conductive oxide, such as SiO_2, in between the semiconductor and the read-out gate electrode. This is useful because it insulates the gate electrode from the source and drain electrodes, increasing performance. This particular schematic shows a NMOS transistor.

which creates a current in the depletion region, resulting again in background noise and dark current, along with the creation of hot pixels, which are individual sensors with higher rates of charge leakage.

Single event effects
Unlike cumulative effects, SEEs are caused by a single particle, making them probabilistic events, meaning that at any given time there is the same chance of one happening during a mission. There are many different types of SEEs, the first being the single-event upset, also called bitflip. The incoming particle strikes an electronic component and creates a free charge, which can then reset a memory bit. The second type is the single-event latch-up, where the incoming particle causes the struck electronic component to freeze and draw excessive current until it is reset or the batteries burn out through thermal runaway. This can heavily damage both the detector and even the current supply [13]. The third type is single-event burnout, which permanently destroys the device by charge accumulation and thus by a high current passing through electronics. The last SEE mentioned here is single-event gate rupture, which creates a conducting path in the gate oxide of metal oxide semiconductor field effect transistors, resulting in permanent detector damage.

2.5   Pixel detectors

If we took a reverse bias p-n detector and were to divide the electron-attracting electrode into a chessboard pattern grid, into pixels, where each electrode would be isolated from the other and have separate readout electronics, we would create a pixel detector. Pixel detectors are sensitive to two-dimensional incoming particle position, and because of the relatively small electrode size, they have a smaller capacitance and thus a smaller leakage current and noise than a single electrode detector of
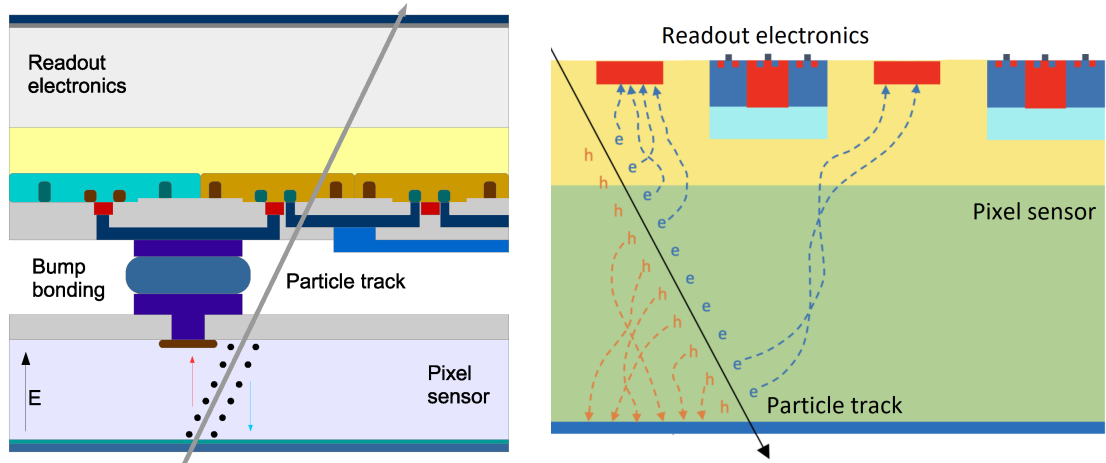
Figure 2.6: Structure comparison of hybrid pixel detectors (left) and monolithic pixel detectors (right). Taken and edited from [32], [33].

larger proportions. Depending on the connection of readout electronics to sensors[1] Depending on the connection of readout electronics to sensors, two main types of pixel detectors can be distinguished. Hybrid pixel detectors have their sensors and electronics on two different wafers, while monolithic pixel sensors have them both in a single layer of material. Hybrid detectors can be more miniaturized than monolithic detectors, but they are also more expensive to manufacture. Both structures can be seen in Fig. 2.6.

2.6   SpacePix-2

SpacePix-2 is a monolithic active pixel detector developed using commercial SoI[2] CMOS[3] technology, in which the detecting sensors are integrated into a thick wafer while readout electronics are integrated into a thin silicon layer, and both layers are separated by the buried oxide layer, BOX. It is designed for in-space dosimetry with the ability to measure energy deposited into the pixels and thus visualize the interacting space radiation in the sensor. The detector consists of an array of $64{\times}64$ square pixels with a 60 µm pitch, resulting in a sensitive area of $3840{\times}3840$ µm^2. SpacePix detectors utilize a bias voltage of 150 V, creating a depleted area approximately 35 µm deep.

The X-CHIP-03 detector demonstrated that monolithic detector technology has a large potential for manufacturing low-power pixelated silicon radiation detectors,

---

[1]Sensors are parts of the detector sensitive to ionization.

[2]Silicon-on-Insulator technology uses a thin silicon layer on top of an insulator to reduce parasitic capacitances of interconnections, to allow more electronics into a smaller space [34], and to reduce the detector's susceptibility to SEEs [35].

[3]Complementary Metal-Oxide-Semiconductor is a type of fabrication process that reduces noise and power consumption.

and it was decided to carry on with the design and production of a new class of detectors optimized for space radiation detection and dosimetry, the SpacePix ASIC family. The spectral and imaging capabilities of X-CHIP-03, which is the predecessor to SpacePix-2, fabricated in the same technology, can be seen in Figures 2.7., 2.8. and 2.9. They show a response to soft X-rays, a proton beam of 150 MeV, and neon and xenon beams. These ion beams from the U400M isochronous cyclotron and Tandetron 4130MC also served as SEU tests, in which no destructive SEEs were observed and the SEU cross section was found to be low with regards to the bulk CMOS [35].
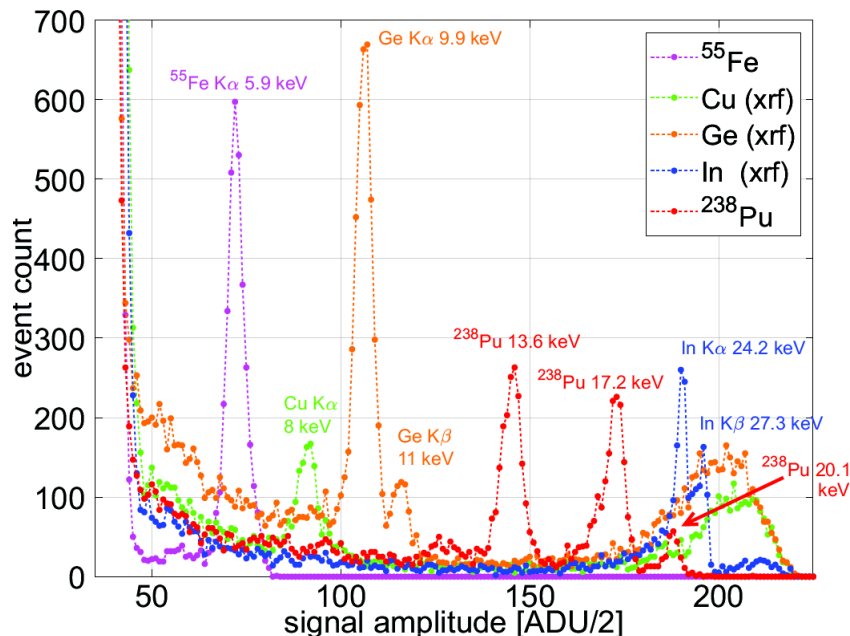
Figure 2.7: An uncalibrated X-CHIP-03 single-pixel response to soft X-rays, generated by the radioactive decay of ^{55}Fe and ^{238}Pu or by the fluorescence of Cu, Ge, and In, showcasing the spectral resolution of X-CHIP-03. Event count peaks corresponding to the energy of the individual Kα and Kβ characteristic X-rays for the aforementioned elements can be seen.

The SpacePix-3 is an evolution of the SpacePix-2, with improvements such as a bug fix for the analog to digital converter, bandgap reference voltage changes, and a new feature that uses defined data sampling at the falling or rising edge.
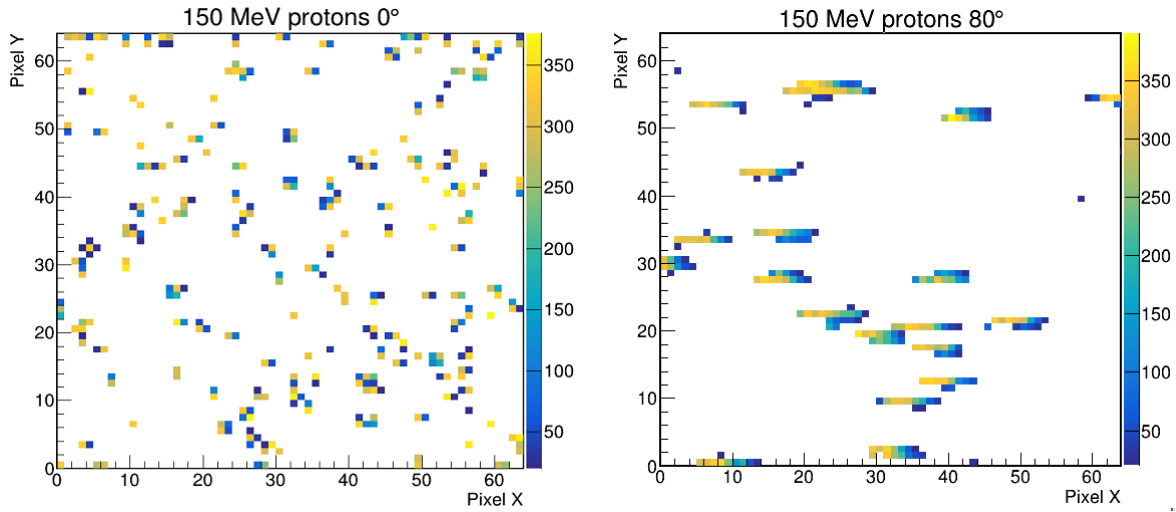
Figure 2.8: Visualisation of a 150 MeV proton beam with the X-CHIP-03 sensor being oriented perpendicular (left) and almost parallel, at 80°(right), to the incoming beam. Perpendicular protons are shown to usually produce single-point clusters, but it is still possible to approximate the point of entry when larger clusters are produced, by comparing the signal amplitudes of hit pixels.
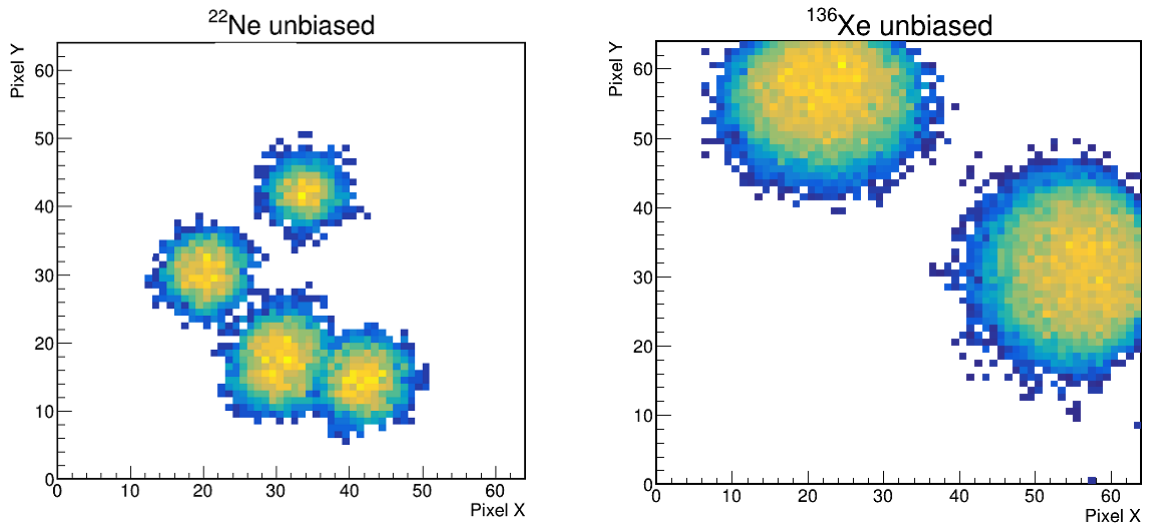

Figure 2.9: Visualization of U400M Ne (left) and Xe (right) beams using the X-CHIP-03 sensor. In comparison to protons in Fig. 2.8, Ne and Xe ions are shown to produce much larger clusters, with Xe clusters being again larger than the ones of Ne origin. This is expected behavior because heavier particles deposit more energy into a material by ionization, as described by Equation 2.1.

Chapter 3

SpacePix-3 HIMAC test beam analysis

3.1 HIMAC

HIMAC, or Heavy Ion Medical Accelerator in Chiba, is a part of the National Institute of Radiological Sciences, NIRS, in Tokyo, Japan. It is capable of accelerating ions ranging from H to Fe to energies of 100 MeV/u to 800 MeV/u. Despite the fact that HIMAC was originally constructed for cancer therapy, numerous particle physics experiments were conducted there. HIMAC was also used for X-CHIP and SpacePix detector testing.

3.2 SpacePix-3 Si beam response

In order to characterize the detection properties of the SpacePix-3 ASIC, an experimental testbeam campaign was devised. An heavy ion beam was chosen to study the effects of signal generation in the depleted and undepleted region of the sensor. In the following text, a description of the experimental procedure and a quick analysis of the data is presented. Measurements were done on HIMAC by irradiating SpacePix-3 with 290 MeV/u Si ions (Si290) in the spring of 2023. The accelerated silicon ions have sufficient energy to penetrate the whole detector and create a large amount of charge carriers which can be used for study. Three different detector orientations to the ion beam were tested: one for a direct hit of 0°, one for a nearly parallel hit of 80°, and one for a parallel hit of 90°. Used detector orientations can be seen in Fig. 3.1. These different angles were chosen to study the cluster properties as a function of depth in the sensor layer of the detector.
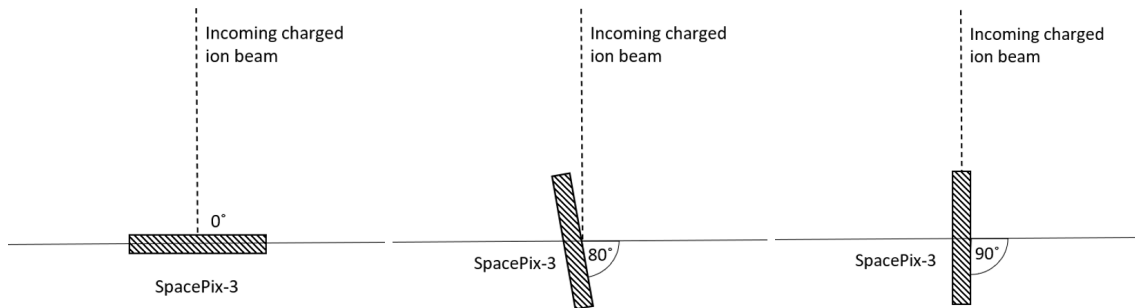
Figure 3.1: Spacepix-3 orientation in regards to the HIMAC charged ion beam.

3.2.1   0°

Detector data for all angles was analyzed using ROOT [36], a C++ library developed by CERN, designed for particle physics data analysis. Figure 3.2 shows clusters created as a response to perpendicular Si ions irradiating the Spacepix-3 sensor. Clusters are sets of in-space adjacent digitized signals generated presumably by the same particle and obtained by a detector at a certain time. Due to the architecture of the SpacePix ASIC, a background subtraction of pixel value is necessary. The background pedestal value represents an output voltage from the pixel when there is no signal from ionizing radiation. A background subtraction procedure was developed which uses averaged pixel data from four previous frames when there was no hit in the pixel. This average value is then subtracted from the following frames, showing only the voltage signal from particle hits. This background subtraction algorithm was used for all beam angles. As expected, the perpendicular beam was creating well-defined, almost circular clusters. The selection of events for different angles can be seen in Appendix 4.4.1.

3.2.2   80°

As the incoming particles reach deeper into the detector and leave the depleted region and its electric field responsible for electron-hole pair movement, the created pairs start to diffuse, reaching the neighboring pixels' electric field. This effect creates a larger signal area than if the particles stopped in the depleted layer, and is more prominent with an angled beam because the drifting charge carriers reach further pixels, which were far from being originally hit by the incoming particle, resulting in a cluster widening with the particle path deeper into the sensor. This phenomenon can be seen in Figures 3.3 and 3.4, showing clusters caused by the particle beam angled at 80°. The narrow initial particle entrance is visible, along with the track broadening as the particle passes through the detector until the induced pairs are too deep to reach the electric field by diffusing, and the signal dissipates. Such track evolution is a wanted behavior because it allows the estimation of the incoming particle direction using the cluster shape.
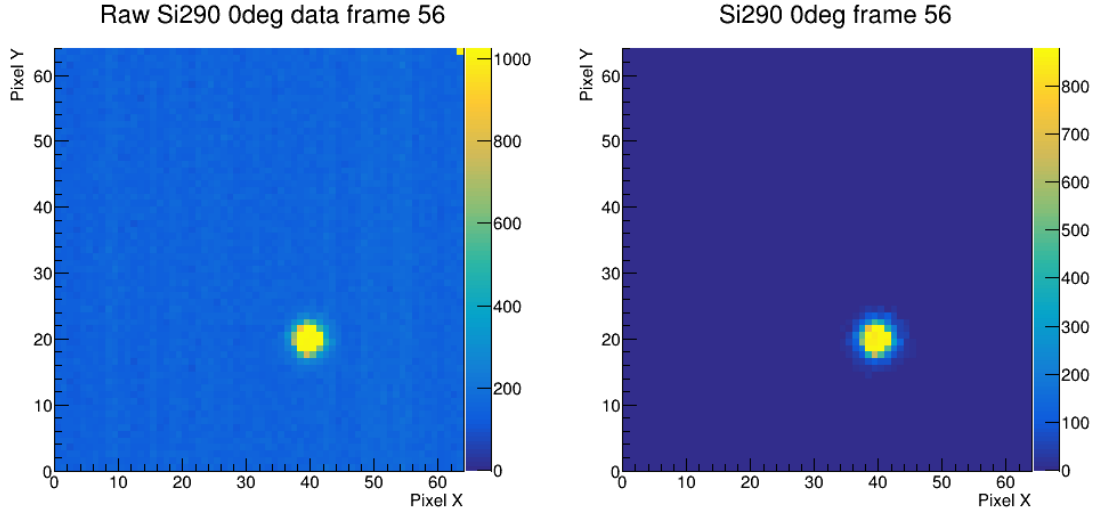
Figure 3.2: Spacepix-3 irradiated by a perpendicular 290 MeV/u Si beam without (left) and with (right) subtracted background. The average cluster size is between 5 to 6 pixels, but no sharp edge of the cluster is visible because the charge carriers outside the depleted region diffuse to the neighboring pixels, inducing a signal there, creating the soft edge of the cluster. This effect is described further in Subsection 3.2.2.

In Fig. 3.4, a signal at the edge of the active detector area is seen. It is induced when a charged particle leaves the detector sensor area while still having enough energy to ionize. Generated charge carriers outside of the depleted area then accumulate at the detector border and create a signal with an intensity similar to the signal at the original particle entry point. This affects the effectiveness of the particle energy measurement and the angle estimation, and thus raises the need for a guard ring in the sensor layer for future chip designs, around edge pixels, to define the electric field region and stop the outside charge carriers from inducing a signal.

3.2.3   90°

With a 90° irradiation, the incoming particle can only pass through the two different detector environments. It can pass through the depleted layer, as shown in Fig. 3.5, or through the diffusion area, as seen in Fig. 3.6. It can also slightly deviate from its path and travel from one environment to another as shown in Fig. 3.7. The signal at the detector edge is also visible using this inclination, both at the particle entry point and at the particle exit point.

The silicon ion test beam validated the SpacePix-3 detectors for use with heavy ions. It also showed that background subtraction algorithms performs satisfactorily. It was found out that SpacePix-3 chips can be improved by the inclusion of field-terminating structures at the edge of the pixel matrix to ensure the proper functionality of the edge pixels.
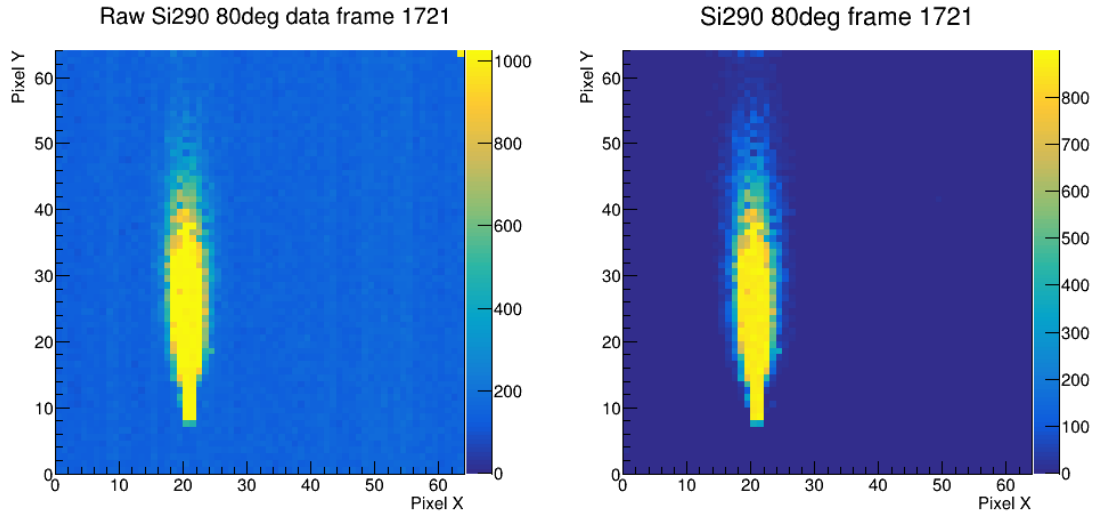
Figure 3.3: SpacePix-3 irradiated by a nearly parallel, 80°, 290 MeV/u Si beam without (left) and with (right) subtracted background. The change in the signal area as the incoming particle passes through the detector body is visible.
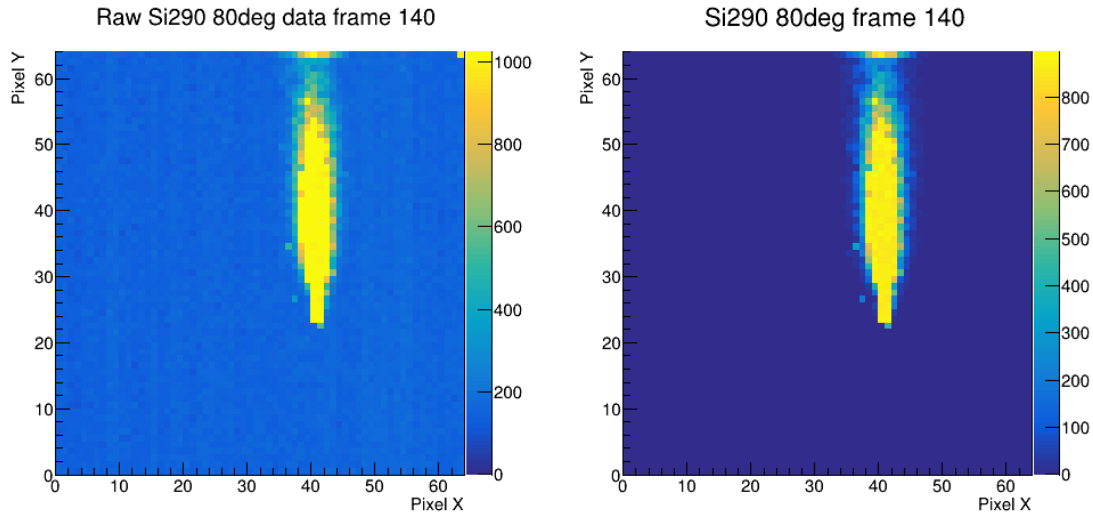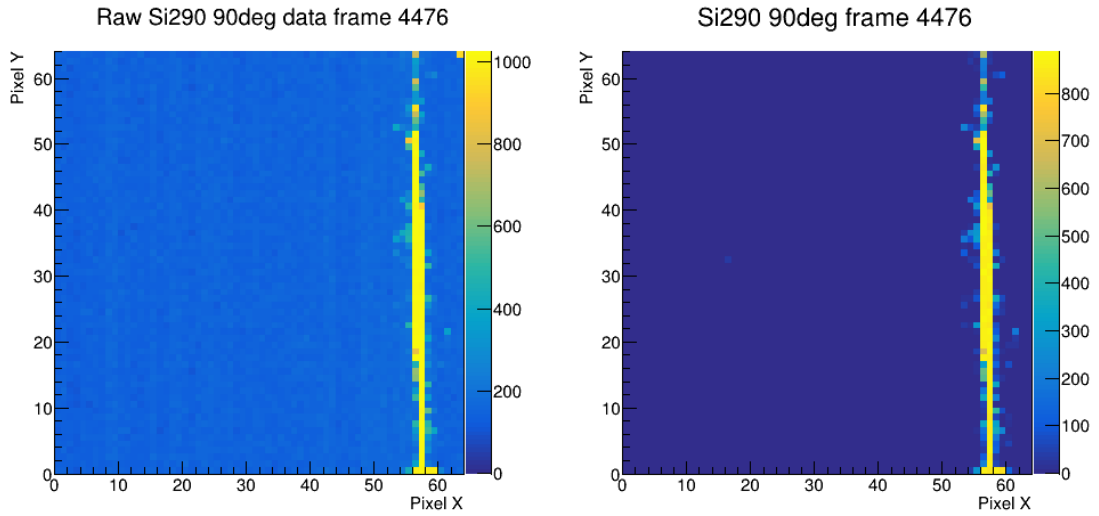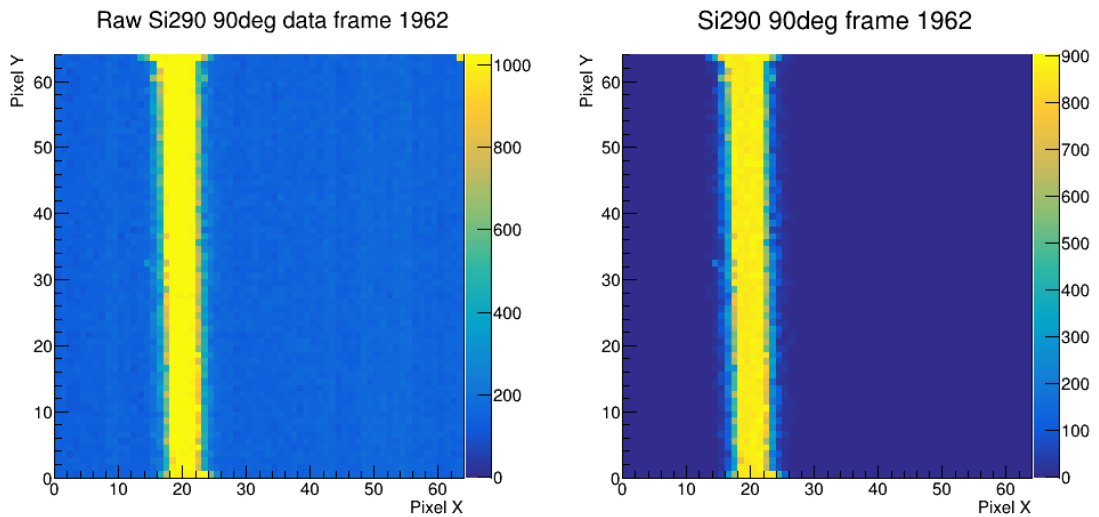

Figure 3.4: SpacePix-3 irradiated by a nearly parallel, 80°, 290/u MeV Si beam without (left) and with (right) subtracted background. Along with the signal widening as the incoming particle reaches the diffusion layer, the signal induced at the edge of the active detector area is visible.
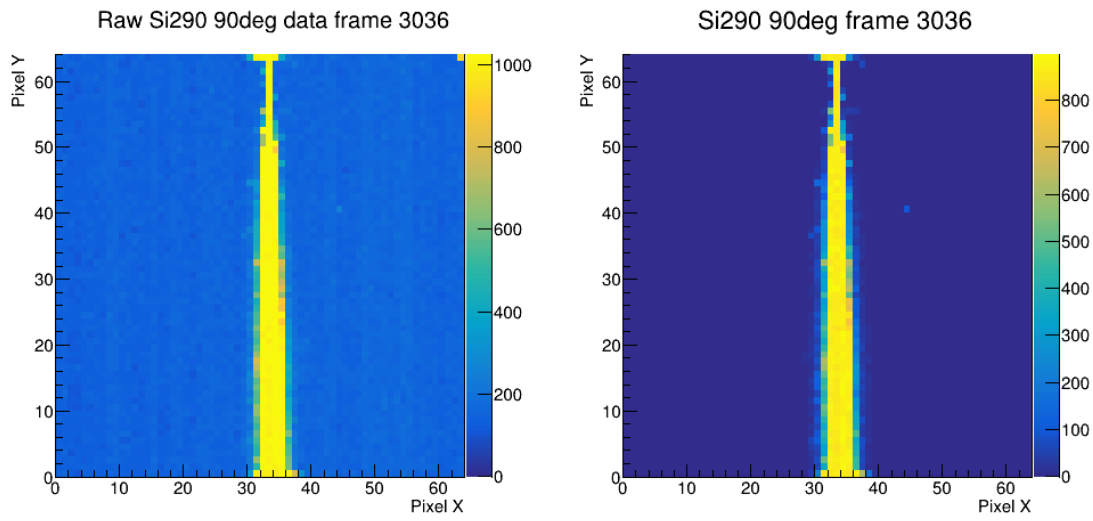
Figure 3.5: SpacePix-3 irradiated by a parallel 290 MeV/u Si beam without (left) and with (right) subtracted background, as the particle passes through the depleted region, possibly partly through the readout electronics. The signal induced at the detector edges, created from the charge carriers generated outside of the active detector area, is visible.

Figure 3.6: SpacePix-3 irradiated by a parallel 290 MeV/u Si beam without (left) and with (right) subtracted background, as the particle passes through the diffusion region. The signal induced at the detector edges, created from the charge carriers generated outside of the active detector area, is visible.

Figure 3.7: SpacePix-3 irradiated by a parallel 290 MeV/u Si beam without (left) and with (right) subtracted background, as the particle passes through the depleted and diffusion region border, due to the angle not being exactly parallel to the detector body. The signal induced at the detector edges, created from the charge carriers generated outside of the active detector area, is visible.

Chapter 4

VZLUSAT-2 orbital SXRM data analysis

4.1   VZLUSAT-2

The VZLUSAT-2 is a Czech technological nanosatellite that was launched in January 2022 onboard the Falcon 9 SpaceX rocket. Its photograph on the construction stand is shown in Fig. 4.1. It is operated by the Czech Aerospace Research Center (VZLU a.s.). It is orbiting in a Sun-synchronous orbit[1], at 500-600 km above sea level, with its main mission being to test satellite technologies for upcoming Czech space missions. It carries several different sensors and detectors, with their functionality ranging from optical Earth imaging using two 1.3 megapixel HD cameras to cosmic gamma-ray burst and X-ray detection. It also carries the 2SD instrument for space dosimetry. Further description is available at [37].

4.2   2SD instrument

2SD, the Space Dosimetry System Demonstrator, is an instrument, developed in co-operation between the FNSPE CTU and the private company esc Aerospace, which consists of the Soft X-ray Monitor, SXM, the SpacepiX Radiation Monitor, SXRM, and the control electronics. The SXRM is a combination of several interleaved layers of SpacePix-2 detectors, along with absorber layers and aluminum shielding, and it is made to monitor the flux, energy, and direction of charged particles [39]. It can be seen in Figure 4.2 and is designed for long-term orbital and interplanetary missions. Visualizations of the SXRM onboard the VZLUSAT-2 data from measurements in the SAA are shown in Fig. 4.3.

---

[1]SSO is an orbit, in which the satellite passes over any planet's surface point always at the same local mean solar time.
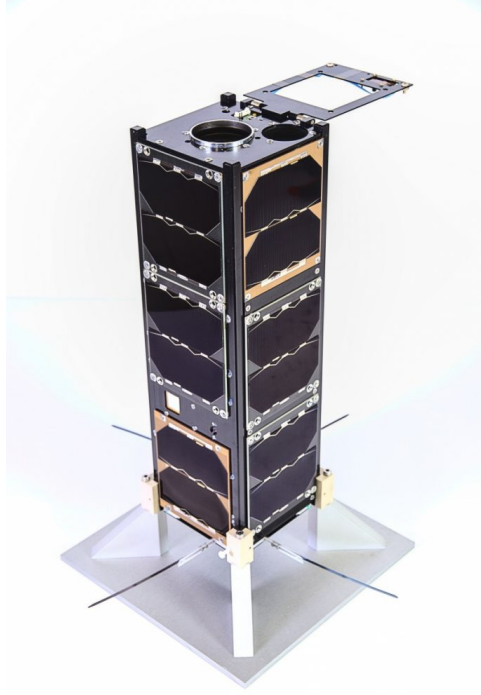
Figure 4.1: Photograph of the VZLUSAT-2 nanosatellite on a testing stand [38].

	Energy range
SXM	
Photons	4 - 20 keV
SXRM	
Electrons	0.1 - 10 MeV
Protons	2 - 400 MeV
Heavy ions	0.5 - 100 $\mathrm{MeV\,cm^2\,mg^{-1}}$

Table 4.1: Energy ranges for particle detection of the SXM and the SXRM.

Energy ranges for particle detection can be seen in Tab. 4.1. It is a radiation monitoring system developed for cubesat PC-104 standard. The 2SD contains a STM32-based microprocessor, which allows for data processing capabilities of the instrument. Its outputs can be configured to be raw data frames, position and total deposited energy in clusters, individual particle track parameters, and histograms of cluster energy deposition in all layers. The histograms are least demanding from the point of view of the required data bandwidth for transfer to the ground.

4.3 SXRM orbital data

After over a year of SXRM commissioning, firmware upgrades, and a calibration campaign, on March 13, 2023, at 08:54:00 UTC, 2SD on VZLUSAT-2 started a
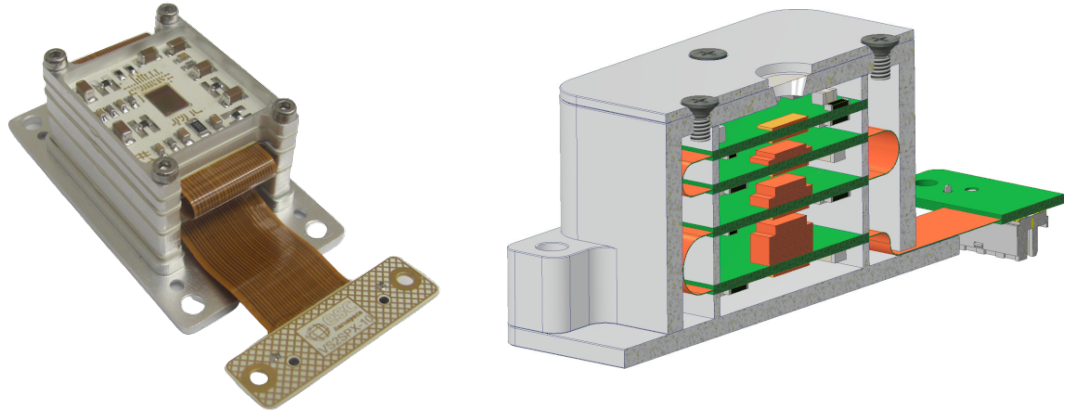
Figure 4.2: The SXRM (left) and the SXRM detector model (right), where green parts are printed circuit boards, orange parts are absorbers, in between which are five SpacePix-2 detectors. The detector is encompassed in an aluminum box with a cutout on top in order to shield incoming particles from all other undesirable directions.
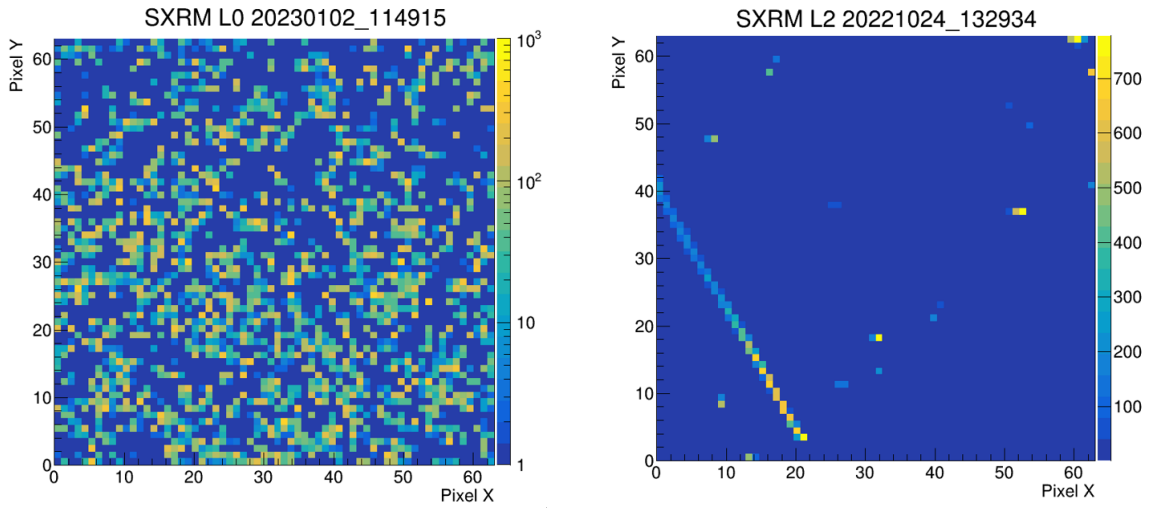

Figure 4.3: Visualization of the data from two layers of the SXRM onboard the VZLUSAT-2 nanosatellite, when passing through the SAA. L0 layer (left) is the layer with no shielding, and thus a large amount of pixel-sized clusters are visible. L2 layer (right) is shielded, resulting in the detection of only more energetic and penetrating particles.

24-hour measurement of the radiation environment in LEO. During this time, it completed its orbit nearly 15 times, with the measurement period being 1 s and the shutter being set to 50 ms. Data histograms of cluster energies were created every 30 s and saved into five CSV files, one for each SXRM layer. Unfortunately, the second layer of SXRM has become inactive after the VZLUSAT-2 launch in 2022 because of a currently unknown cause. More on this in Section 4.4.

The data collection was supposed to end on March 14, 2023 09:00:00 UTC but the last histogram was created at 08:48:01 UTC. This implies, that there was a time deviation between the OBC planner and the onboard clock of 00:11:59. The cause of this complication was a crystal oscillator responsible for keeping track of time for the whole satellite. It ticks 8300 ppm slower in a vacuum than in air. While nearly 12 minutes in a day may not seem relevant, VZLUSAT-2 moves approximately 5500 km during this time interval, thus making its position-sensitive data unserviceable. To account for the slower clock on the satellite, a linearly increasing time shift had to be added to each time measurement. If a linear clock drift rate was assumed, accurate timestamps thus had to be calculated using the linear approximation formula

$$t_{real,i} = t_{meas,i} + i\frac{\Delta t}{N}, \tag{4.1}$$

where $t_{real,i}$ is the real time, $t_{meas,i}$ is the time measured by the satellite, $\Delta t \approx 12$ minutes is the time shift, i is the index of measurement and N is the total number of measurements.

The adjusted timestamps were then used to calculate accurate at-time coordinates using the VZLUSAT-2 two-line element set, TLE, with an epoch date being 13.03.2023 and a Python package Skyfield. Skyfield is a Python astronomy package for generating high-precision positions of planets and satellites [40] and TLE is a data format encapsulating elements for orbital description for a given point in time called the epoch. Two more Python packages, Matplotlib [41] and Cartopy [42], were then used to plot the number of clusters as a 2D histogram of coordinates. This was done for all four functioning layers of SXRM. Results for the first and last layers can be seen in Fig. 4.4 and the remaining two layers can be seen in Appendix 4.4.1.

In the ground track plot for the first layer of SXRM, SENSOR-0, both the South Atlantic Anomaly and the outer radiation belt can be seen, with the center of the SAA being in the middle of the Atlantic Ocean and the outer belt being at around 60th parallel north and 50th parallel south. In the ground track plot for the last layer of SXRM, SENSOR-4, however, the outer radiation belt disappears and the center of the SAA moved above South America, as anticipated in Fig. 1.6. This is caused by the shielding of deeper parts of SXRM, which restricts low-energy particles and outer belt electrons from passing into further layers. These plots show the ability of SpacePix-2 to map out the SAA along with the rest of the radiation environment in LEO while being smaller, lighter, having lower power consumption, and having

a larger energetic range than other commercially available pixel detectors, such as TimePix3 [43] and MediPix3 [44].

4.4 Future for SpacePix detectors

The performance of the SpacePix detectors shown in Chapters 3 and 4, along with their small size and low power consumption, make them ideal for the increasingly popular CubeSat type satellites and other nanosatellites. Due to the long mission duration and the near impossibility of repairing faulty instruments during them, the whole apparatus must function flawlessly. For this reason, the failure of the second layer of SXRM, L1, on VZLUSAT-2 needs to be properly investigated. Diagnostic showed that the L1 layer is detecting particles but does not send out a signal. Before launch, the detector was tested for stronger vibrations than the ones created by the Falcon 9 rocket launch, and thus mechanical vibrations are excluded from possible causes. Other causes are to be examined. The main motivation for preventing issues such as this is the upcoming LVICE^2 mission, which makes use of SpacePix-3 detectors, and its unimpaired functionality is a must for the upcoming years of research.

4.4.1 LVICE^2 mission

LVICE^2 stands for Lunar VIcinity Complex Environmental Explorer and as the name suggests, this mission is about exploring the Moon and its vicinity. It is the first proposed Czech lunar mission, combining the efforts of several Czech companies and academic institutions for Czechia to become one of the few countries that have ever reached the Moon. Its success also solidifies Czechia as a reliable partner for future ESA missions. Preliminary probe design can be seen in Fig. 4.5. Three faculties of the Czech Technical University take part in the LVICE^2 mission, with the Faculty of Mechanical Engineering having responsibility for the mission design, astrodynamics, and thermal modeling, the Faculty of Electrical Engineering having responsibility for fluxgate magnetometers as a part of the scientific payload, and the Faculty of Nuclear Sciences and Physical Engineering having responsibility for radiation simulation and protection, piezoelectric foil dust detectors, and the SXRM.

The planned trajectory of the LVICE^2 is shown in Fig. 4.6. The mission has two main phases, each corresponding to a different part of the trajectory and a different scientific goal. The LVICE^2 mission's unique orbit will periodically pass through interplanetary space and the tail of the Earth's magnetosphere. It will allow it to study several space environments, such as interplanetary space, areas affected by the Earth's magnetosphere, such as foreshock, bow shock, the far-Earth magnetotail, and low lunar orbit. The goals of the mission are to measure dust concentration, monitor the solar wind's long-term properties, and study the plasma turbulence processes
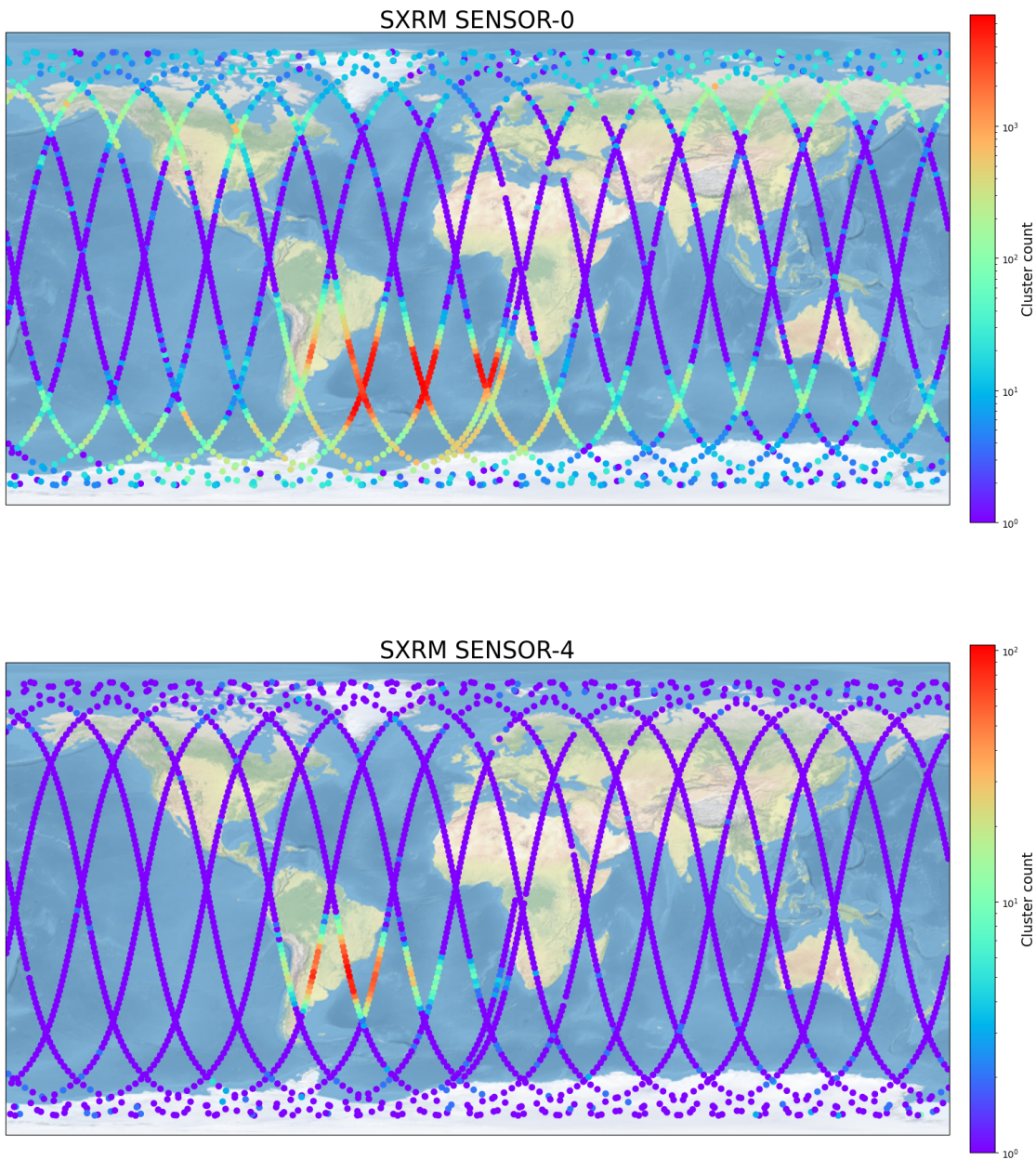
Figure 4.4: Number of clusters detected by the first (SENSOR-0) and the last (SENSOR-4) layer of SXRM on VZLUSAT-2 during its 24 h measurement period shown as a ground track plot with a logarithmic z-axis.
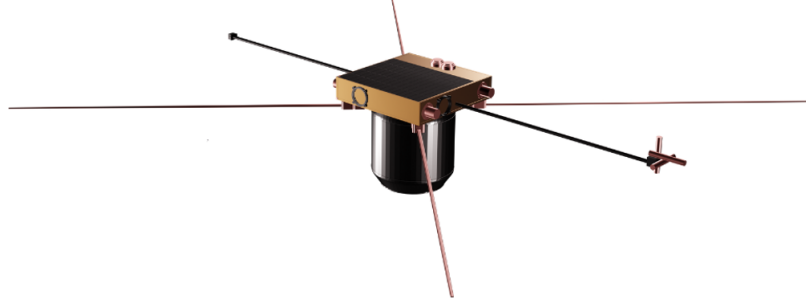
Figure 4.5: Preliminary visualisation of LVICE^2, June 2023.

in the solar wind in order to provide insights into how solar wind turbulence heats the solar wind at larger distances from the Sun and how the solar wind interacts with the Moon's surface and in the lunar wake. After launch and transfer to the elliptical lunar orbit, the first part of the LVICE^2 mission scientific program will commence. For about a year, the probe will orbit the Moon and study its space environment. After that, another burn will get it on the distant retrograde orbit, DRO. Then, after entering the DRO, the main objective will swerve towards the observation of Kordylewski dust clouds, which are large concentrations of dust that possibly exist at the L4 and L5 Lagrangian points, places where the gravitational pulls from two massive bodies are equal. During the mission, measurements of the energetic particle spectra will also take place, as one of the significant risks for human spaceflight beyond Earth's protective magnetosphere is exposure to ionizing radiation in cislunar space. This will be the first recent mission to study the spectra of secondary particles created on the lunar surface.

Many scientific instruments play a key role in fulfilling the scientific goals of the mission, from foil dust detectors for quantifying the dust density, through multiple magnetometers a Faraday Cup Analyzer for parametrizing the solar wind, to two ionizing radiation detectors. One of these is the PARDAL^2, or PArticle Radiation Detector At Lunar orbit and Lagrange points. It consists of two different detector systems: a scintillator-based RADIVA neutron and gamma energy photon spectrometer and the SXRM.

All of these devices will be encased in a 66x66x61 cm^3 probe body, and along with solar panels, three 100 Wh battery modules, and hydrazine thrusters as a propulsion system, its mass will come to approximately 60 kg without fuel or 140 kg with fuel. The B1 study phase was finished in June 2023, and the launch is currently set for 2028.
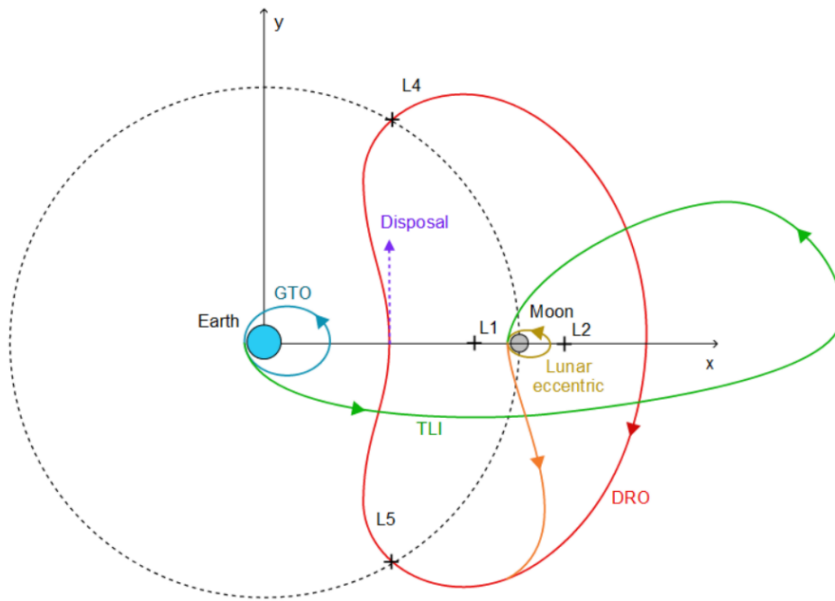
Figure 4.6: LVICE² mission design trajectory visualization [45]. After launch, the probe will orbit in the geostationary transfer orbit, GTO, for approximately a week (blue), after which the trans-lunar injection maneuver, TLI, takes place to set the probe on its journey (green). After 90 days, the spacecraft will reach the lunar orbit utilising ballistic capture, and it will stay there approximately for the next year (orange). The final phase of the mission starts by transitioning from the lunar eccentric orbit to the distant retrograde orbit, DRO, where it will stay for the next year with the possibility of extension (red).

Conclusions

The goal of this thesis was to introduce the subject of the space environment and spacecraft operation, to describe the operational principles of semiconductor detectors, namely the SpacePix detectors, and to analyze data from the latest SpacePix experiments, along with showcasing the effectiveness of SpacePix detectors for future space missions, such as LVICE^2.

An analysis of the SpacePix-3 response to a HIMAC test beam was performed. Signal clusters generated by the detector for three different incoming beam inclinations, 0°, 80°, and 90°, were shown and discussed. Signal generation on the border of the active detector area was highlighted, and the need for adding an edge guard ring for future versions of the SpacePix monolithic pixel detector was proposed.

After over a year of preparations, the VZLUSAT-2 nanosatellite generated its first data, which was analyzed in this work. Ground track plots of a 24 h measurement for all operating layers of SXRM were presented, together with a discussion of reasons for one SXRM layer to be non-functioning and an explanation of a time shift caused by the properties of the time tracking oscillator crystal operating in a vacuum. The functionality of the SpacePix-2 chip and SXRM in the space environment has been demonstrated by observing the Van Allen radiation belts and the South Atlantic Anomaly. These observation results are comparable to those of other existing detectors, with SpacePix detectors being smaller, lighter, and less power-consuming, all valued properties in space missions.

The results of this work will help in designing the subsequent evolutions of the SpacePix-3 detector. They will also serve as a demonstration of the imaging capabilities of the SpacePix chips. In the future, more data from the VZLUSAT-2 will be available, the effectiveness of the guard ring will be trialed, and more showcases of the SpacePix-3 applicability for future space missions will be performed.

Bibliography

[1] Y. Lu, Q. Shao, H. Yue, and F. Yang, "A review of the space environment effects on spacecraft in different orbits," *IEEE access*, vol. 7, pp. 93473–93488, 2019.

[2] R. Eastes, S. Solomon, R. Daniell, D. Anderson, A. Burns, S. England, C. Martinis, and W. McClintock, "Global-scale observations of the equatorial ionization anomaly," *Geophysical Research Letters*, vol. 46, no. 16, pp. 9318–9326, 2019.

[3] S. Zhang, J. Shi, and J. Wang, "Satellite on-board failure statistics and analysis," *Spacecraft Engineering*, vol. 19, no. 4, pp. 41–46, 2010.

[4] W. Schimmerling and S. B. Curtis, "Workshop on the radiation environment of the satellite power system," tech. rep., California Univ., Berkeley (USA). Lawrence Berkeley Lab., 1978.

[5] M. S. Longair, *High energy astrophysics*. Cambridge university press, 2010.

[6] "Solar Cosmic Rays." `https://astronomy.swin.edu.au/cosmos/s/Solar+Cosmic+Rays`. [Online; accessed 2-August-2023].

[7] Z.-N. Shen, G. Qin, P. Zuo, and F. Wei, "Modulation of galactic cosmic rays from helium to nickel in the inner heliosphere," *The Astrophysical Journal*, vol. 887, no. 2, p. 132, 2019.

[8] W. Bietenholz, "The most powerful particles in the universe: a cosmic smash," *arXiv preprint arXiv:1305.1346*, 2013.

[9] D. Baker, J. Blake, L. Callis, J. Cummings, D. Hovestadt, S. Kanekal, B. Klecker, R. Mewaldt, and R. Zwickl, "Relativistic electron acceleration and decay time scales in the inner and outer radiation belts: Sampex," *Geophysical Research Letters*, vol. 21, no. 6, pp. 409–412, 1994.

[10] J. Heirtzler, "Future radiation damage in space due to the south atlantic anomaly. nasa/goddard space flight center greenbeld-usa. pp: 1-12.-kallenrode mb 2004. space physics," 1997.

[11] "Wikipedia Commons." `https://commons.wikimedia.org/w/index.php?title=File:Van_Allen_radiation_belt.svg&oldid=472621960`. [Online; accessed 2-August-2023].

[12] C. C. Finlay, C. Kloss, N. Olsen, M. D. Hammer, L. Tøffner-Clausen, A. Grayver, and A. Kuvshinov, "The chaos-7 geomagnetic field model and observed changes in the south atlantic anomaly," *Earth, Planets and Space*, vol. 72, no. 1, pp. 1–31, 2020.

[13] J. R. Wertz, D. F. Everett, and J. J. Puschell, "Space mission engineering: the new smad," *(No Title)*, 2011.

[14] C. A. Belk, *Meteoroids and orbital debris: effects on spacecraft*, vol. 1408. National Aeronautics and Space Administration, Marshall Space Flight Center, 1997.

[15] D. J. Kessler and B. G. Cour-Palais, "Collision frequency of artificial satellites: The creation of a debris belt," *Journal of Geophysical Research: Space Physics*, vol. 83, no. A6, pp. 2637–2646, 1978.

[16] "About space debris." `https://www.esa.int/Space_Safety/Space_Debris/About_space_debris`. [Online; accessed 2-August-2023].

[17] "Distribution of space debris in orbit around Earth." `https://www.esa.int/ESA_Multimedia/Videos/2019/02/Distribution_of_space_debris_in_orbit_around_Earth`, note = "[Online; accessed 2-August-2023]".

[18] "Space debris: Assessing the risk." `https://www.esa.int/About_Us/ESOC/Space_debris_assessing_the_risk`. [Online; accessed 2-August-2023].

[19] J. Liu, G. Li, Z. H. Zhu, and X. Zhan, "Orbital boost characteristics of spacecraft by electrodynamic tethers with consideration of electric-magnetic-dynamic energy coupling," *Acta Astronautica*, vol. 171, pp. 196–207, 2020.

[20] A. N. Cox, *Allen's astrophysical quantities*. Springer, 2015.

[21] B. A. Banks, S. K. Miller, K. K. deGroh, and R. Demko, "Atomic oxygen effects on spacecraft materials," in *Ninth International Symposium on Materials in a Space Environment*, no. NASA/TM-2003-212484, 2003.

[22] "Advanced Aerospace Medicine Online." `https://www.faa.gov/about/office_org/headquarters_offices/avs/offices/aam/cami/library/online_libraries/aerospace_medicine/tutorial/media/III.4.1.2_The_Space_Environment.pdf`. [Online; accessed 2-August-2023].

[23] D. B. Contreira, F. Rodrigues, K. Makita, C. Brum, W. Gonzalez, N. Trivedi, M. Da Silva, and N. Schuch, "An experiment to study solar flare effects on radio-communication signals," *Advances in Space Research*, vol. 36, no. 12, pp. 2455–2459, 2005.

[24] S. A. Jyothi, "Solar superstorms: planning for an internet apocalypse," in *Proceedings of the 2021 ACM SIGCOMM 2021 Conference*, pp. 692–704, 2021.

[25] B. G. Streetman, S. Banerjee, *et al.*, *Solid state electronic devices*, vol. 4. Prentice hall New Jersey, 2000.

[26] Z. Weinberg, G. Rubloff, and E. Bassous, "Transmission, photoconductivity, and the experimental band gap of thermally grown si o 2 films," *Physical Review B*, vol. 19, no. 6, p. 3107, 1979.

[27] "Energy band diagram of semiconductors, insulators and metals." `https://www.eeeguide.com/energy-band-diagram-of-semiconductors-insulators-and-metals/`. [Online; accessed 2-August-2023].

[28] H. Spieler, *Semiconductor detector systems*, vol. 12. Oxford university press, 2005.

[29] P. D. Group, R. Workman, V. Burkert, V. Crede, E. Klempt, U. Thoma, L. Tiator, K. Agashe, G. Aielli, B. Allanach, *et al.*, "Review of particle physics," *Progress of theoretical and experimental physics*, vol. 2022, no. 8, p. 083C01, 2022.

[30] D. Durini and D. Arutinov, "Operational principles of silicon image sensors," in *High Performance Silicon Imaging*, pp. 25–73, Elsevier, 2020.

[31] E. Secretariat, "Methods for the calculation of radiation received and its effects, and a policy for design margins," *European Cooperation for Space Standardization, Noordwijk*, 2008.

[32] R. Marco-Hernández, "Overview of cmos sensors for future tracking detectors," *Instruments*, vol. 4, no. 4, p. 36, 2020.

[33] L. De Cilladi, T. Corradino, G.-F. Dalla Betta, C. Neubüser, and L. Pancheri, "Fully depleted monolithic active microstrip sensors: Tcad simulation study of an innovative design concept," *Sensors*, vol. 21, no. 6, p. 1990, 2021.

[34] G. Lutz *et al.*, *Semiconductor radiation detectors*. Springer, 2007.

[35] M. Marcisovska, T. Benka, M. Finger, M. Havranek, M. Hejtmanek, Z. Janoska, A. Kabatova, V. Kafka, M. Marcisovsky, S. V. Mitrofanov, *et al.*, "A study of single event effects induced by heavy charged particles in 180 nm soi technology," in *2018 IEEE Nuclear Science Symposium and Medical Imaging Conference Proceedings (NSS/MIC)*, pp. 1–4, IEEE, 2018.

[36] R. Brun and F. Rademakers, "Root—an object oriented data analysis framework," *Nuclear instruments and methods in physics research section A: accelerators, spectrometers, detectors and associated equipment*, vol. 389, no. 1-2, pp. 81–86, 1997.

[37] "VZLUSAT-2, Czech technological nanosatellite." `https://www.vzlusat2.cz/en/`. [Online; accessed 2-August-2023].

43

[38] "VZLUSAT-2 is ready to obtain precise images of the Earth." `https://www.vzlu.cz/vzlusat-2-is-ready-to-obtain-precise-images-of-the-earth/?lang=en`. [Online; accessed 2-August-2023].

[39] "The SpacePix radiation monitor, SXRM." `https://indico.esa.int/event/233/attachments/3219/4238/The__SpacePix_radiation_monitor-Matej_Vaculciak.pdf`. [Online; accessed 2-August-2023].

[40] B. Rhodes, "Skyfield: High precision research-grade positions for planets and earth satellites generator," *Astrophysics Source Code Library*, pp. ascl–1907, 2019.

[41] J. D. Hunter, "Matplotlib: A 2d graphics environment," *Computing in Science & Engineering*, vol. 9, no. 3, pp. 90–95, 2007.

[42] Met Office, *Cartopy: a cartographic python library with a Matplotlib interface*. Exeter, Devon, 2010 - 2015.

[43] T. Poikela, J. Plosila, T. Westerlund, M. Campbell, M. De Gaspari, X. Llopart, V. Gromov, R. Kluit, M. Van Beuzekom, F. Zappon, *et al.*, "Timepix3: a 65k channel hybrid pixel readout chip with simultaneous toa/tot and sparse readout," *Journal of instrumentation*, vol. 9, no. 05, p. C05013, 2014.

[44] R. Ballabriga, M. Campbell, E. Heijne, X. Llopart, L. Tlustos, and W. Wong, "Medipix3: A 64 k pixel detector readout chip working in single photon counting mode with improved spectrometric performance," *Nuclear Instruments and Methods in Physics Research Section A: Accelerators, Spectrometers, Detectors and Associated Equipment*, vol. 633, pp. S15–S18, 2011.

[45] "LVICE², Lunar VIcinity Complex Environmental Explorer." `https://www.lvice2.cz/`. [Online; accessed 2-August-2023].

Attachments
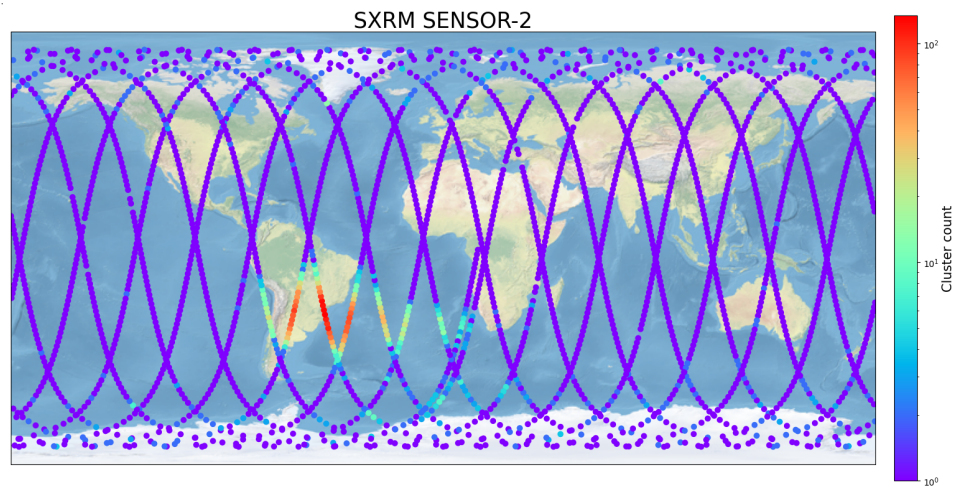
Figure 7: Number of detected clusters ground track plot of the SENSOR-2 in the SXRM. The disappearance of the outer belt and the SAA shift, in comparison to SENSOR-0, is visible.
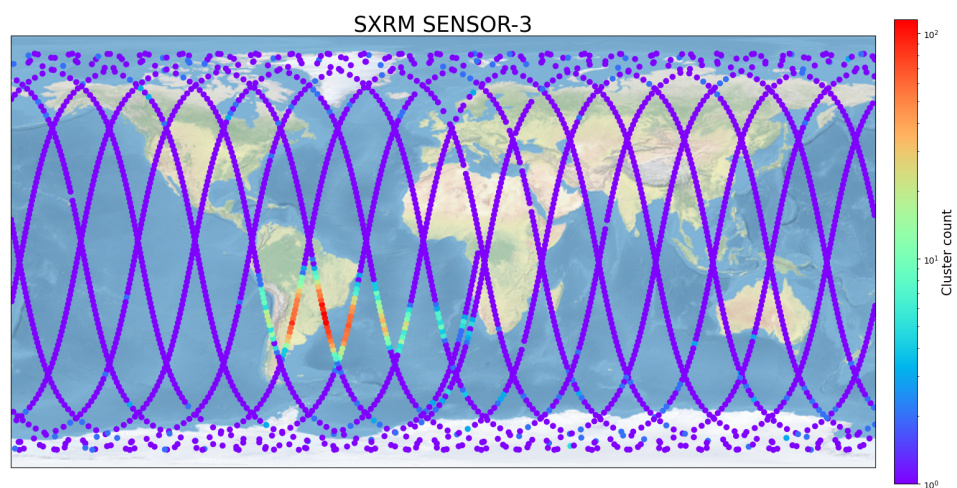

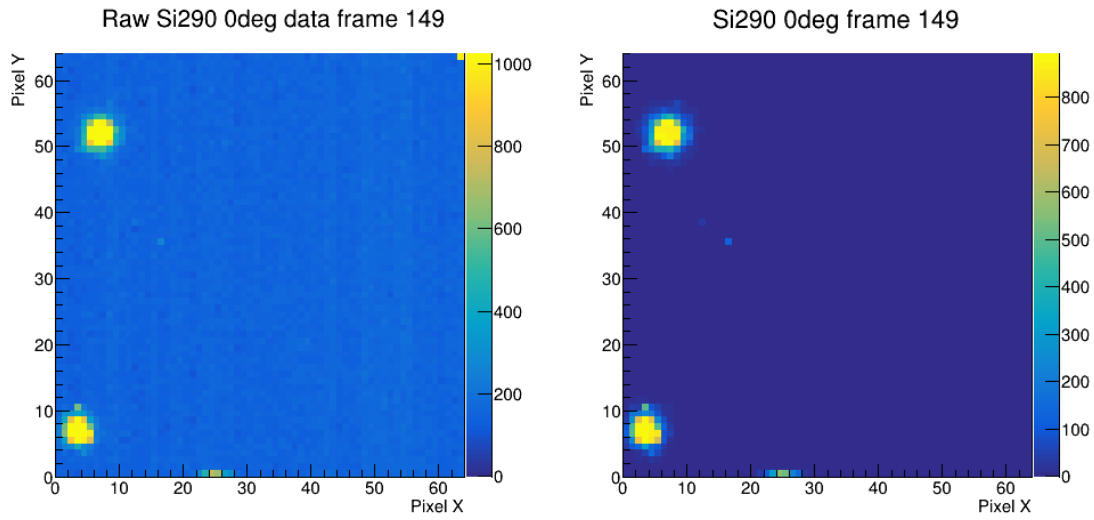Figure 8: Number of detected clusters ground track plot of the SENSOR-3 in the SXRM.

Figure 9: Spacepix-3 irradiated by a perpendicular 290 MeV/u Si beam without (left) and with (right) subtracted background.
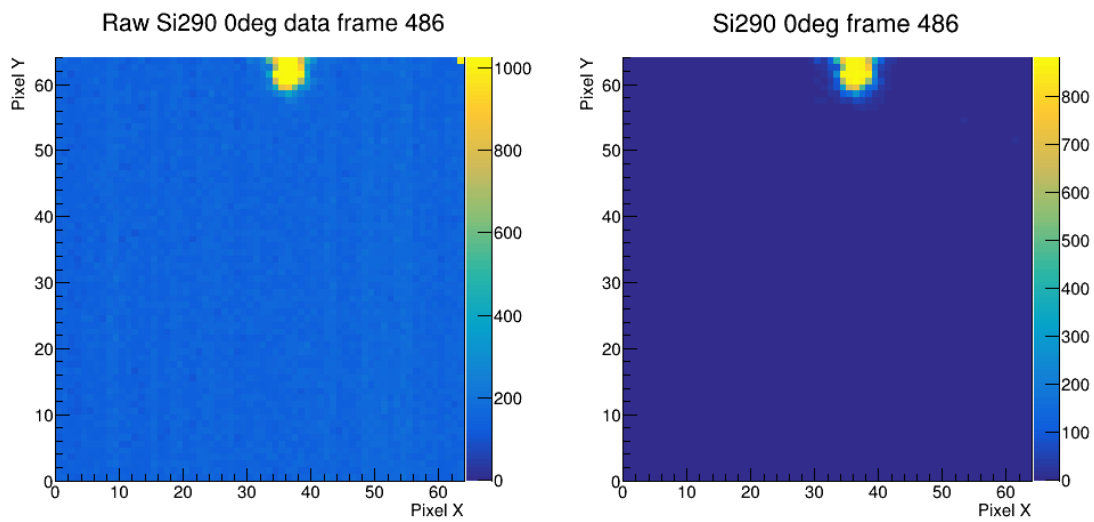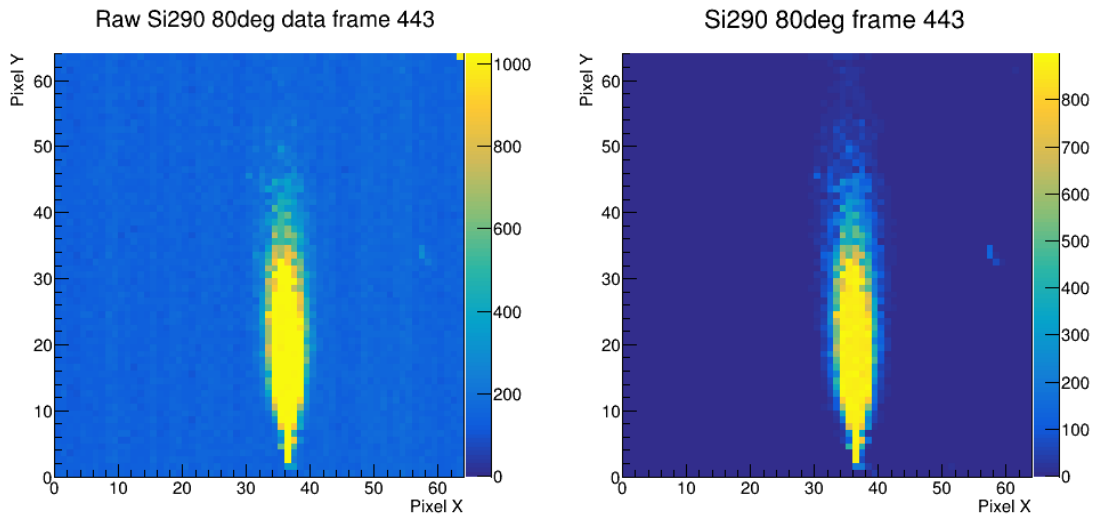

Figure 10: Spacepix-3 irradiated by a perpendicular 290 MeV/u Si beam without (left) and with (right) subtracted background. The signal at the edge of the active detector area is visible.
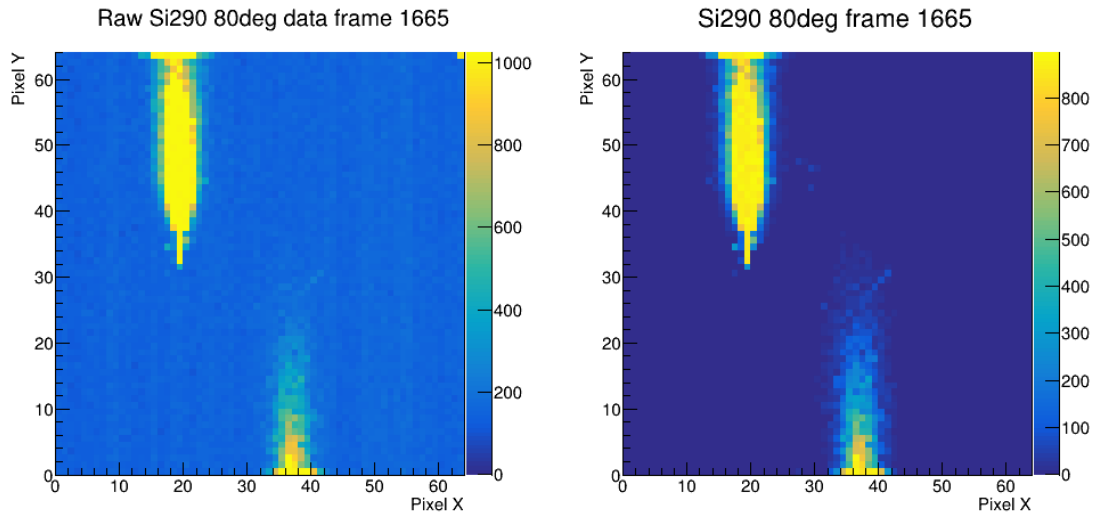
Figure 11: SpacePix-3 irradiated by a nearly parallel, 80°, 290 MeV/u Si beam without (left) and with (right) subtracted background.
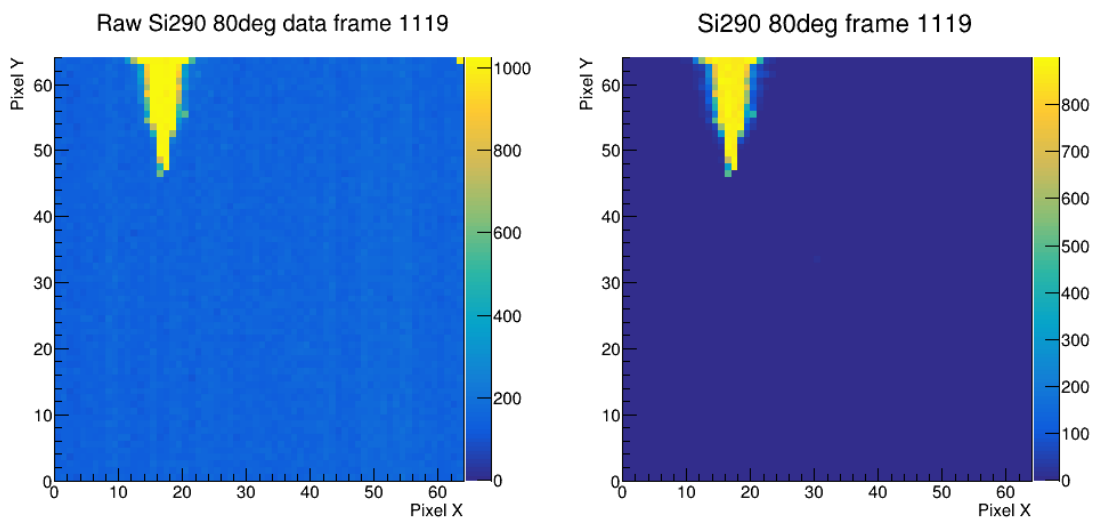
Figure 12: SpacePix-3 irradiated by a nearly parallel, 80°, 290 MeV/u Si beam without (left) and with (right) subtracted background. The signal at the edge of the active detector area is visible.
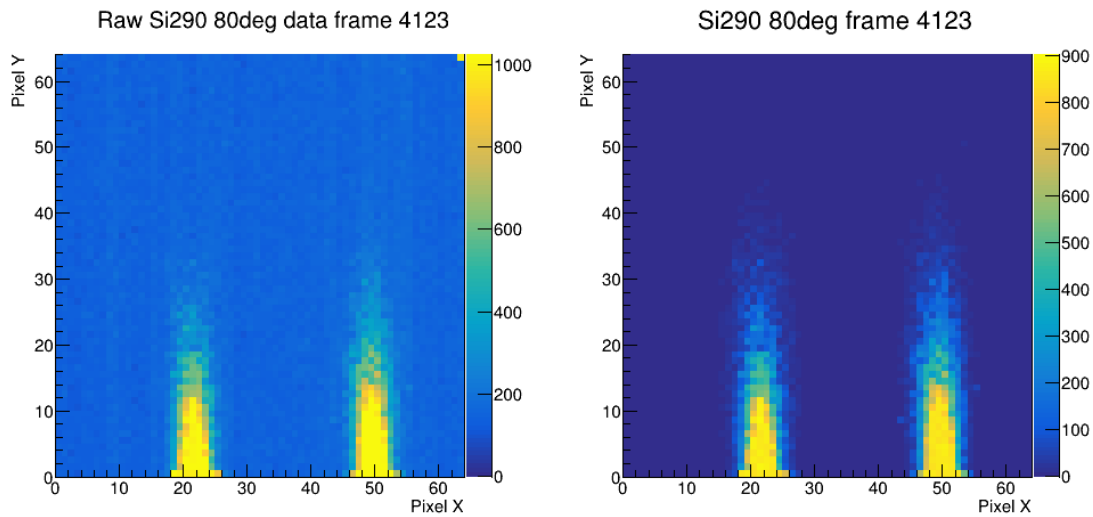
Figure 13: SpacePix-3 irradiated by a nearly parallel, 80°, 290 MeV/u Si beam without (left) and with (right) subtracted background. The signal at the edge of the active detector area is visible.
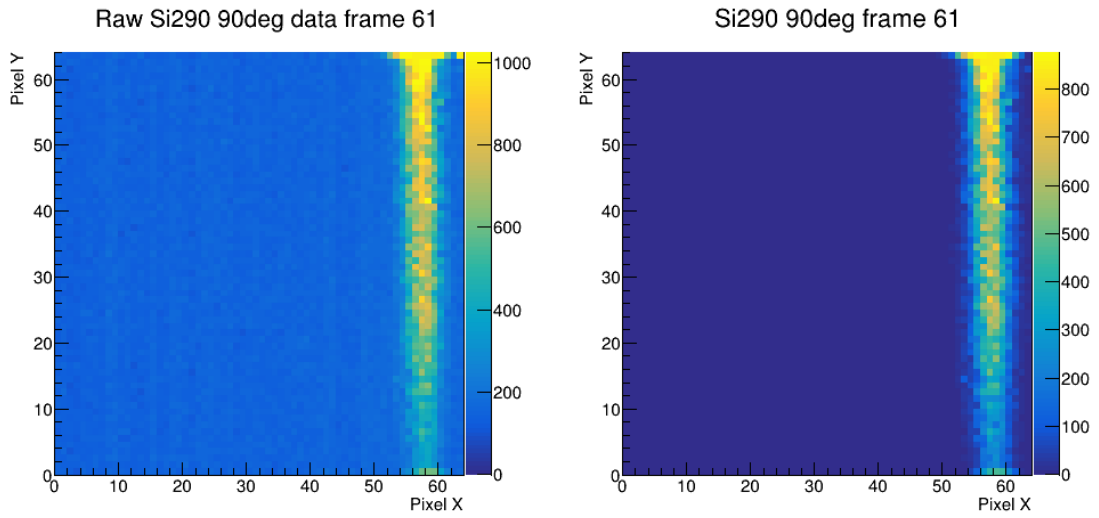

Figure 14: SpacePix-3 irradiated by a nearly parallel, 80°, 290 MeV/u Si beam without (left) and with (right) subtracted background. The signal at the edge of the active detector area is visible.

Figure 15: SpacePix-3 irradiated by a parallel 290 MeV/u Si beam without (left) and with (right) subtracted background, as the particle passes through the diffusion region. The signal at the edge of the active detector area is visible.
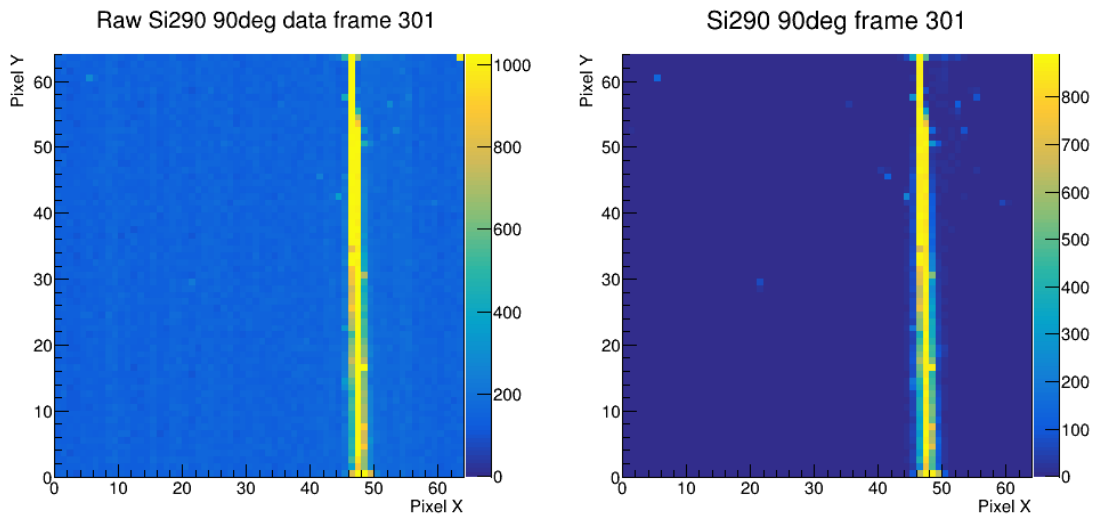

Figure 16: SpacePix-3 irradiated by a parallel 290 MeV/u Si beam without (left) and with (right) subtracted background, as the particle passes through the depleted region. The signal at the edge of the active detector area is visible.
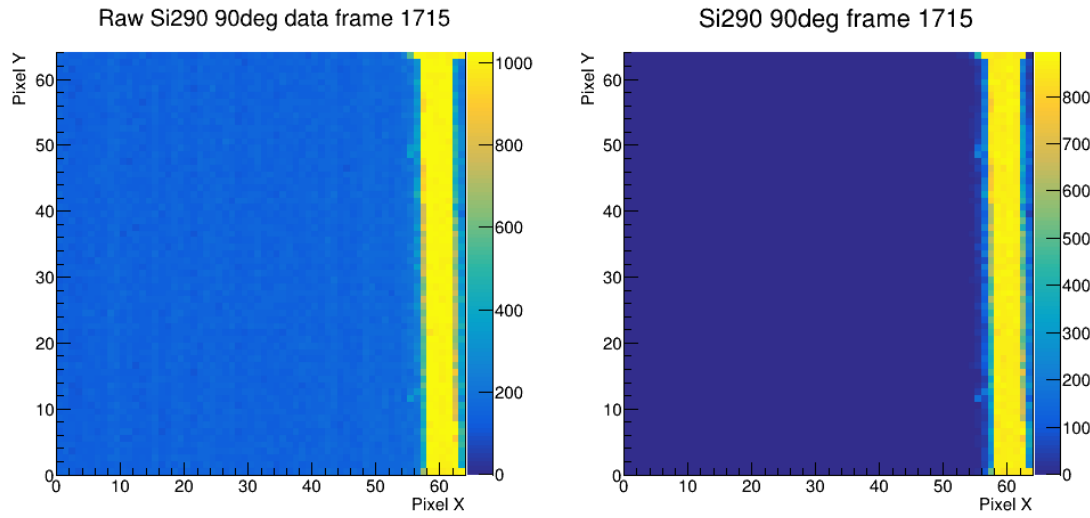
Figure 17: SpacePix-3 irradiated by a parallel 290 MeV/u Si beam without (left) and with (right) subtracted background, as the particle passes through the diffusion region. The signal at the edge of the active detector area is visible.
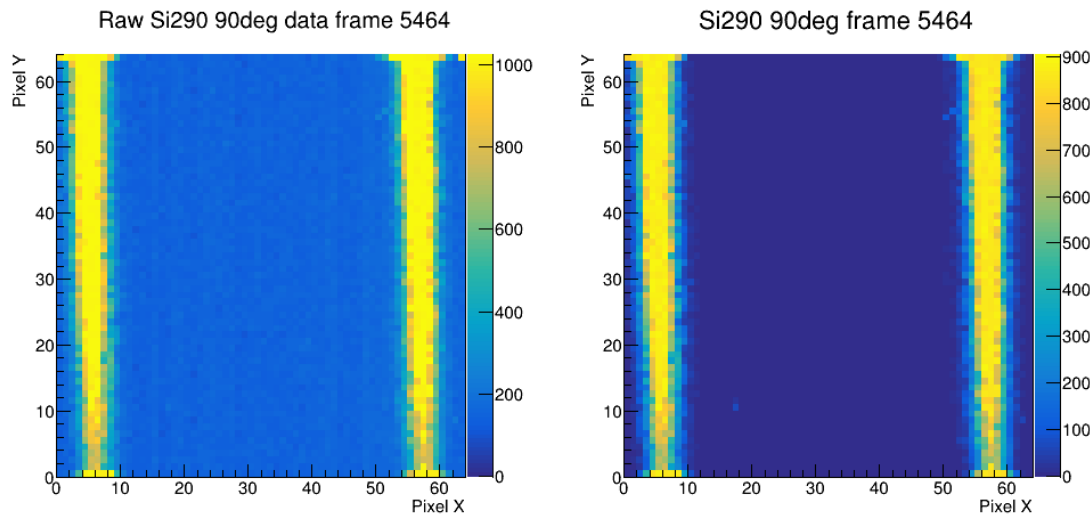

Figure 18: SpacePix-3 irradiated by a parallel 290 MeV/u Si beam without (left) and with (right) subtracted background, as the particle passes through the diffusion region. The signal at the edge of the active detector area is visible.